

Article

Probability Density Components Analysis: A New Approach to Treatment and Classification of SAR Images

Osmar Abílio de Carvalho Júnior ^{1,*}, Luz Marilda de Moraes Maciel ²,
Ana Paula Ferreira de Carvalho ², Renato Fontes Guimarães ¹, Cristiano Rosa Silva ¹,
Roberto Arnaldo Trancoso Gomes ¹ and Nilton Correia Silva ³

¹ Departamento de Geografia, Campus Universitário Darcy Ribeiro, Universidade de Brasília (UnB), Asa Norte, Brasília, DF 70910-900, Brazil; E-Mails: renatofg@unb.br (R.F.G.); lincecado@hotmail.com (C.R.S.); robertogomes@unb.br (R.A.T.G.)

² Instituto Nacional de Colonização e Reforma Agrária, Coordenação-Geral de Meio Ambiente DTM, SBN Quadra 1, bloco D, Ed. Palácio do Desenvolvimento, Brasília, DF 71670-020, Brazil; E-Mails: marildamaciel@gmail.com (L.M.M.M.); anapaula.fcarvalho@gmail.com (A.P.F.C)

³ Faculdade de Engenharias do Gama, Universidade de Brasília (UnB), Gama, DF 72444-240, Brazil; E-Mail: niltoncs@unb.br

* Author to whom correspondence should be addressed; E-Mail: osmarjr@unb.br; Tel.: +55-61-3367-5001.

Received: 30 September 2013; in revised form: 3 March 2014 / Accepted: 6 March 2014 /

Published: 1 April 2014

Abstract: Speckle noise (salt and pepper) is inherent to synthetic aperture radar (SAR), which causes a usual noise-like granular aspect and complicates the image classification. In SAR image analysis, the spatial information might be a particular benefit for denoising and mapping classes characterized by a statistical distribution of the pixel intensities from a complex and heterogeneous spectral response. This paper proposes the Probability Density Components Analysis (PDCA), a new alternative that combines filtering and frequency histogram to improve the classification procedure for the single-channel synthetic aperture radar (SAR) images. This method was tested on L-band SAR data from the Advanced Land Observation System (ALOS) Phased-Array Synthetic-Aperture Radar (PALSAR) sensor. The study area is localized in the Brazilian Amazon rainforest, northern Rondônia State (municipality of Candeias do Jamari), containing forest and land use patterns. The proposed algorithm uses a moving window over the image, estimating the probability density curve in different image components. Therefore, a single input image generates an output with multi-components. Initially the multi-components should be treated by

noise-reduction methods, such as maximum noise fraction (MNF) or noise-adjusted principal components (NAPCs). Both methods enable reducing noise as well as the ordering of multi-component data in terms of the image quality. In this paper, the NAPC applied to multi-components provided large reductions in the noise levels, and the color composites considering the first NAPC enhance the classification of different surface features. In the spectral classification, the Spectral Correlation Mapper and Minimum Distance were used. The results obtained presented as similar to the visual interpretation of optical images from TM-Landsat and Google Maps.

Keywords: Amazon forest; ALOS; PALSAR; frequency histogram

1. Introduction

The presence of speckle noise (salt and pepper) in synthetic aperture radar (SAR) images causes a usual noise-like granular aspect, which complicates the direct image classification. Thus, a basic problem in SAR image analysis is to develop accurate models for the statistics of the pixel intensities in order to obtain procedures for denoising and classification. Several techniques intend to acquire a stationary model for distinct land cover typologies of image data, eliminating the variations in the scene caused by the presence of surface roughness, topography and the dielectric constant, among others. The stationary assumption is most feasible from a set of pixels of the same land cover class.

One of the main strategies used in SAR image classification is to apply a preprocessing step by speckle filtering, such as the median filter [1,2], the Lee Sigma filter [3–5], and the minimum-mean-square-error (MMSE) filter [6,7], among others. Thus, different filters for SAR images calculate a specific estimator that describes the data distribution pattern of different classes [8].

Another approach is the use of the Probability Density Function (PDF) for the discrimination of different types of distributed scatters [9]. PDF models consider either parametric or nonparametric estimation. Examples of the parametric methods are lognormal [10], Weibull [11], Fisher [12,13], maximum likelihood (ML) [14,15], method of moments (MoM) [13,14] and the generalized Gaussian model [16]. As nonparametric methods, the following can be cited: standard Parzen window estimators [17], artificial neural networks (ANNs) [18], and support vector machines (SVMs) [19]. Different models may be used jointly, considering dictionary-based stochastic expectation maximization (DSEM), particularly necessary in the case of heterogeneous images [20]. However, several parametric families are effective only for specific types of land cover and the search for the best PDF model has a high computational cost. Furthermore, the research that usually adopts the PDF model considers very large regions containing different targets.

This paper aims to propose a method that combines filtering and probability density to improve the classification procedure for single-channel SAR image. In particular, we focus on the frequency histogram, which is the most basic spatial information to describe the distributed SAR scattering. The area occupied by the vertical bars of a histogram gives an idea of the probability, since the sum of the areas of all the bars represents 100% of the data. Therefore, the division of the histogram classes by the total number of samples used provides a probability density concerning the distribution of radar data

for the target. The proposed algorithm uses a moving window method, which calculates the probability density curve and records each histogram category on a specific image component. Thus, a single input image generates different output image components. Each output component represents a determinate category of the histogram, so the spectrum (the z component of the image) shows the data distribution curve for the central pixel of the window. This histogram curve can be classified according to the methods of a spectral classifier, such as the Spectral Angle Mapper (SAM) [21], the Spectral Correlation Mapper (SCM) [22] or the minimum distance. Therefore, this article uses a direct comparison of probability density curves between the reference and image data instead of determining the best PDF model for single-channel SAR.

The study area is located in the Amazon rainforest, where the acquisition of optical images without cloud cover and adequate sunlight is very difficult. This restriction is the main incentive for the use of synthetic aperture radar (SAR) images for the Amazon rainforest, which can be acquired independently of sunlight or cloud cover. Thus, SAR images offer the potential for continuous monitoring of the Amazon forest cover.

2. Study Area

The study area is located in the northern Rondônia State, in the municipality of Candeias do Jamari, 20 km from the capital Porto Velho, (8°29'06"S–9°26'85"S latitudes and 63°42'59"W–63°48'15"W longitudes) (Figure 1). Rondônia State has had a recent history of high rates of deforestation. This area was chosen because of its typical features, such as primary forest and land use patterns.

The area has a tropical rainforest climate, with a dry season from June to August, and a wet season from December to March [23]. The temperature oscillates between 21 °C and 32 °C, with an annual average of 25.5 °C. The relative humidity varies from 74% to 90.8%, with an annual average of 82% [24].

The study area shows both large and continuous forest as regions that were deforested over the years, mostly because of the occupation of subsistence agriculture and livestock. Therefore, the area has pasture, agriculture, secondary vegetation and regeneration in the pasture. Furthermore, the study site is bounded to the west by the reservoir of Samuel Hydroelectric, which is the largest artificial lake in the state with a flooded area of 584.6 km² and a mean depth of around 6 m. The altitude in the dam center is 87 m above sea level. Occupation occurred around the center of the municipality, accessible areas using the road, as well as along the Samuel Reservoir. The rapid conversion of forests causes generalized habitat fragmentation [25,26].

3. Methodology

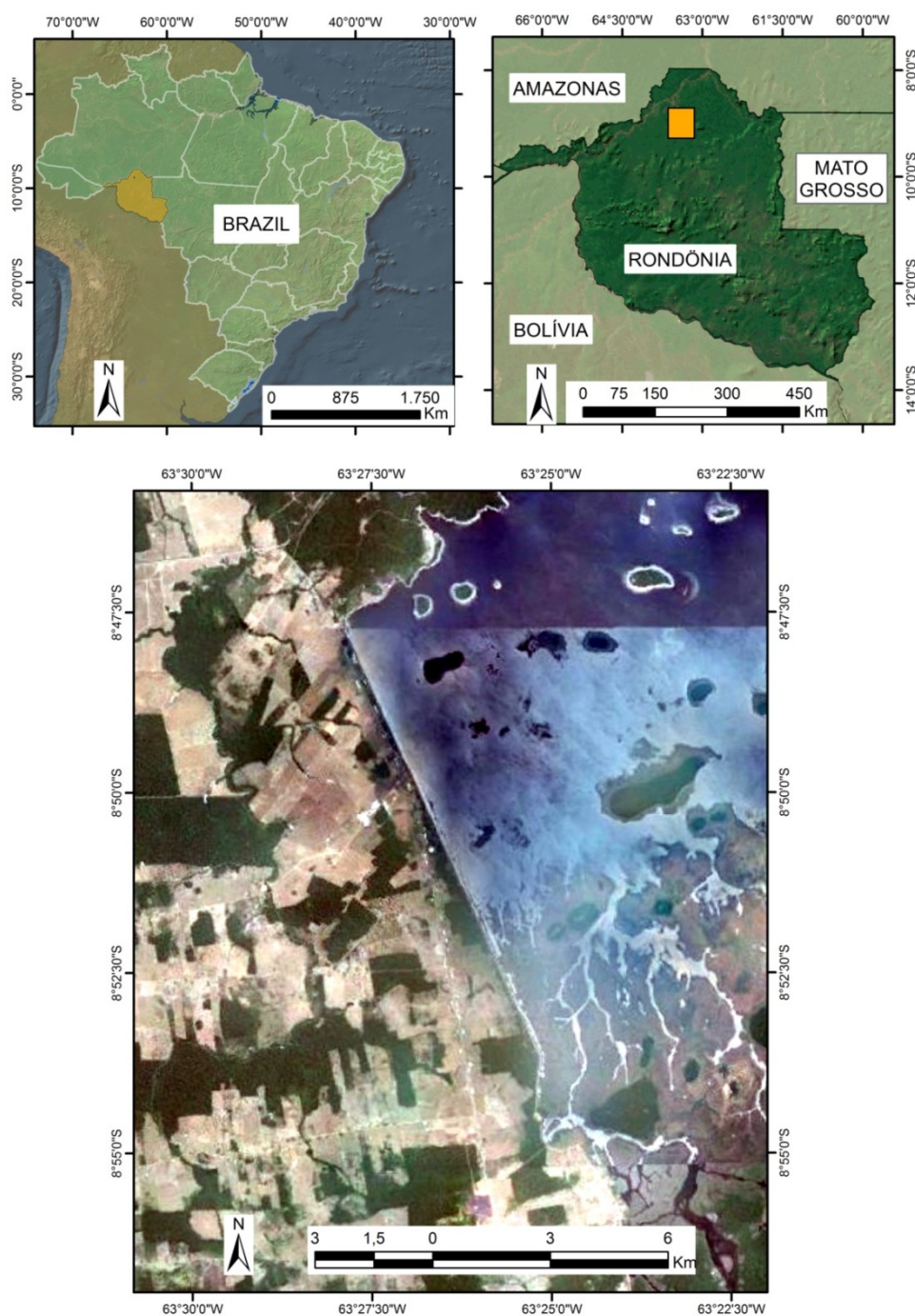
3.1. Datasets for Experiments

In 2006, the Japan Aerospace Exploration Agency (JAXA) launched the Advanced Land Observing Satellite (ALOS), carrying the Phased Array L-Band Synthetic Aperture Radar (PALSAR). In this study, L-band SAR data were acquired from the ALOS-PALSAR sensor over the test site on 19 June 2009 in Fine Beam Dual polarization (FBS; look angle: 34.3°, HV and HH polarization) and processing level 1.5 (the image, including the geo-reference and geo-code) with pixel spacing of 12.5 m. The output image was in Geographic Tagged Image File Format (GeoTIFF) format projected

to the Universal Transverse Mercator (UTM) coordinate system and World Geodetic System 84 (WGS84) datum.

The PALSAR instrument provides enhanced sensor characteristics, including full polarimetry, variable off-nadir viewing, and Scan SAR operations, as well as significantly improved radiometric and geometric performance. It is a fully polarimetric instrument, which operates in the L-band with 1270-MHz (23.6 cm) center frequency and 14- and 28-MHz bandwidths [27]. PALSAR images are widely used in studies of the Amazon forest [28,29].

Figure 1. Study location in the municipality of Candeias do Jamari, RO.

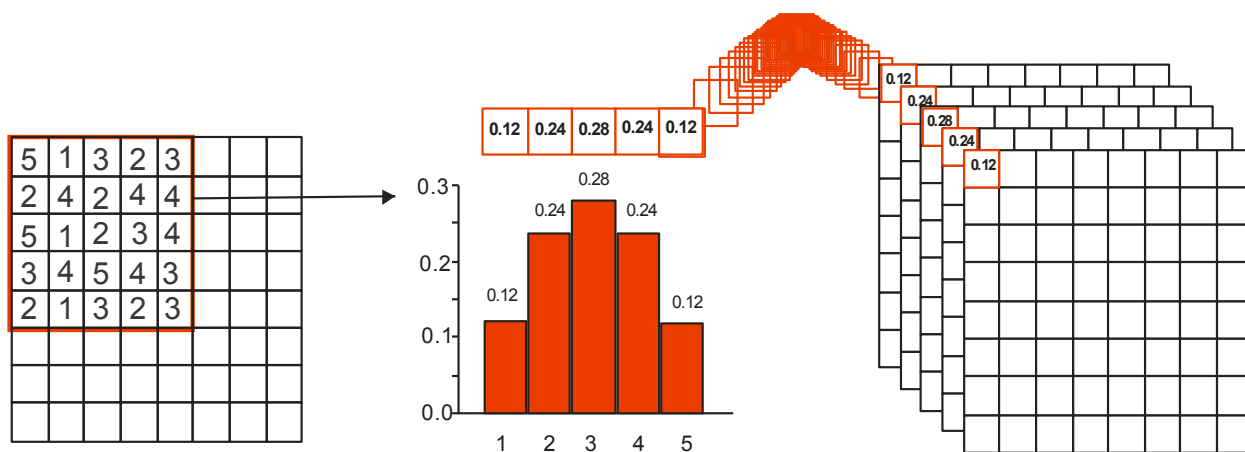


3.2. Probability Density Components Analysis

The histogram is a graphical representation of the frequency distribution, showing the number of observations present in a given category (known as bins). The division of the total number of samples in each bin generates a probability density graph. The sum of all the bins becomes equal to one.

This paper introduces the probability density component analysis (PDCA) method, which calculates the frequency histogram for a moving window and distributes the value of each category in a specific image. Thus, a sequence of images is generated, where the total number of images is equal to the number of histogram bins (Figure 2).

Figure 2. Procedures to generate the Probability Density Components: establishment of a moving window (for example, with a dimension of 5×5), calculating the frequency histogram, and the establishment of images of the probability density components.



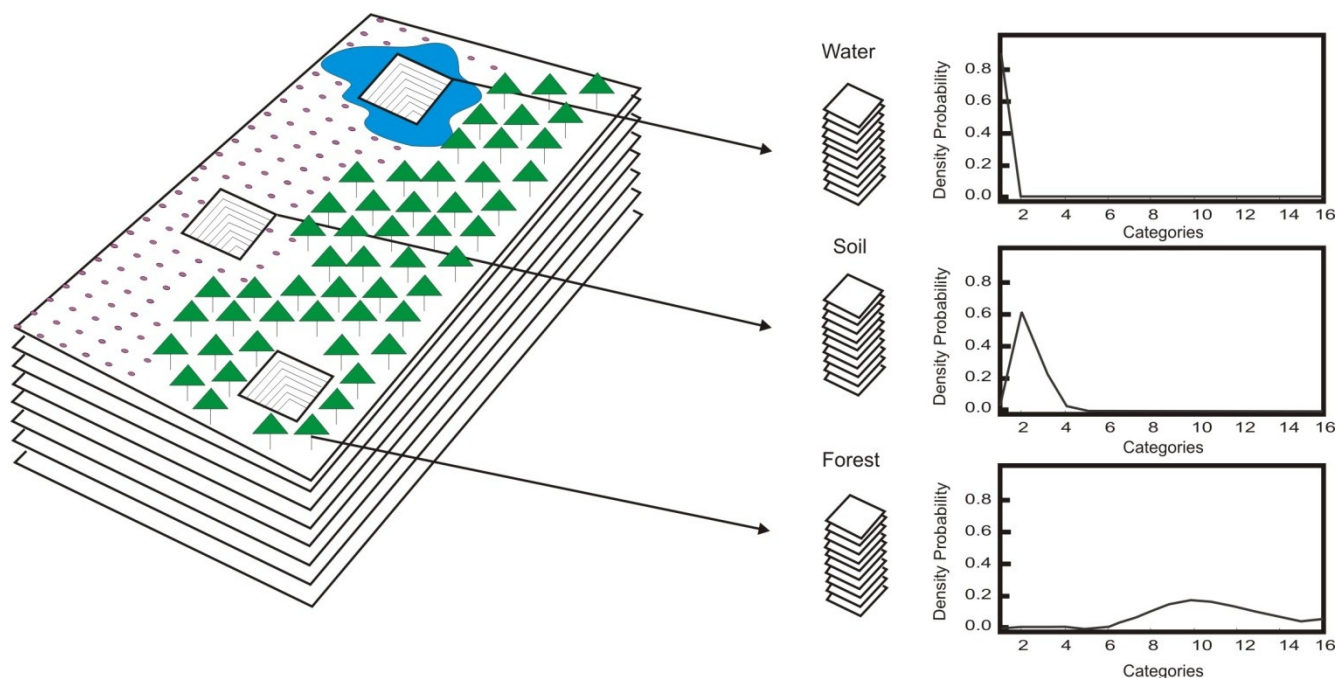
The proposed methodology considers the following input variables: (a) the number of histogram bins (*i.e.*, the number of probability density components); and (b) the window size. The number of histogram bins for the SAR image must be compatible with the window size in order to allow an accumulation of pixels in the discrete intervals, forming a distribution curve. If the number of bins is overestimated, the data distribution is very sparse, not generating a curve. The number of histogram bins can be defined from linear stretches of the number of levels. In this method, a reduction in the radiometric resolution must be performed in order to obtain the probability density curves for moving windows. Thus, the number of grey levels present in an image should be around 16 levels or four bits. Normally, the histogram shows a density estimate, where the speckles are positioned on the tails of distributed radar reflectivity. Therefore, the interference from noisy values (with very high or low) can be avoided by considering linear stretches with a 2% clip on both of the histogram tails.

The window size is the total number of data present in the probability density curve. The best window size should be evaluated according to the data in the study. The increase in the window size causes a decrease in spatial resolution. In contrast, the decrease of the window size can cause a sparse data distribution in the probability density curve.

Similarly, for the design of a hyperspectral cube [30], it is possible to describe a PDCA cube, where instead of the spectral signature, a density of probabilities signature is shown (Figure 3). The probability density may have a treatment for the noise, similar to the spectral data. In the hyperspectral

data, linear transformation techniques are often used to eliminate noise, such as Maximum Noise Fraction (MNF) [31] and Noise-Adjusted Principal Components (NAPCs) [32]. However, these methods are also adequate to eliminate noise interferences of a larger amount of data, such as an aerial gamma-ray survey [33,34] and a time series of remote sensing data [35–37].

Figure 3. The concept of probability density component analysis is shown with a spectrum calculated for each spatial element in an image. The curve describe different targets.



The MNF transform adopts similar arguments to the PCA to derivate its components. This method is a linear transformation that uses a signal-to-noise ratio to sort images, *i.e.*, considering the image quality [31]. MNF calculates a signal-to-noise index, differently from PCA, which uses a variance-covariance matrix of the dataset. Consequently, MNF components will show steadily increasing image quality, unlike the usual ordering of principal components.

NAPC transform is mathematically equivalent to MNF transform, but the former transform can be implemented using standard principal components algorithm, without the need for matrix inversion and eigenanalysis of a nonsymmetric matrix [32]. The application of the NAPC transform requires knowledge of the noise covariance matrix of the data. The noise reference can be obtained from the images by using the Maximum Autocorrelation Factor (MAF) [38]. Spatial covariance (SC_D) is defined as the covariance matrix between the original image, represented by $I(x)$, and the same image, $I(x + D)$, shifted by an amount “ D ”. The noise covariance matrix (NCM_N) can be estimated using the following equation:

$$NCM_N = 1/2SC_D \tag{1}$$

where

$$SC_D = (I(x) - I(x + D)) (I(x) - I(x + D))^{-1} \tag{2}$$

In this algorithm, a “D” equal to 1 was used. The SC_D can be calculated considering shifts from one of eight neighbor directions or by the average of two to eight directions given by the user, according to Equation (3),

$$SC_D = MNCM = (\sum NCM_i)/n \quad (3)$$

where, $MNCM$ is an average spatial covariance of the directions selected; “ i ” is the direction of nearest neighbors (1–8), and “ n ” is the number of directions chosen by the user. Thus, the SC_D matrix is obtained and applied in the steps of the NAPC transform. However, noise removal is only performed with the inverting NAPC transform. During the inversion, the elimination of noisy bands is required using only signal bands. This procedure reduces noise in the original data space.

3.3. Endmember Identification

The endmembers consist of pure elements in the image that, by mixing, form all other spectra present. The techniques for endmember detection were developed for hyperspectral sensors, but have been employed for multispectral sensors and are used in this study on the PDCs. The algorithms used to detect the endmembers implicitly or explicitly assume the convex geometry and the linear mixing model [39–43]. Endmembers present in the scene should be found at the corners of the simplex.

The most widely used algorithm is the method proposed by Boardman and Kruse [44] implemented in the Environment for Visualizing Images (ENVI) [45]. This method has three steps: (a) spectral data reduction, (b) spatial data reduction, and (c) manual identification. This methodology eliminates the redundant factors, such as spatial and spectral, that do not change the set of feasible solutions for the endmembers. In the present study, we performed a spectral reduction data by NAPC and a manual identification using the n-dimensional scatter plot.

3.4. Spectral Classifier

The spectral classifiers compare image spectra to a reference spectrum from spectral libraries or to spectral endmembers [46]. In this paper, we used the following methods: Minimum Distance and SCM [22]. SCM is an improvement of the SAM [21]. SAM has the following problems: it is unable to detect anti-correlated data, and correlation is sensitive to offset factors. The SCM method corrects this limitation because it adopts the Pearson’s correlation. The SCM value varies between -1 and 1 , with 1 meaning that the two series are identical, 0 meaning they are completely uncorrelated, and -1 meaning they are perfect opposites. The major difference between the correlation methods is that SAM uses integral values for X and Y , while SCM uses centered data ($X - X$ mean) and ($Y - Y$ mean). Thus, the cosine correlation is equivalent to the uncentered version of Pearson correlation assuming that the mean of the population is zero. This normalization makes the SCM better than SAM for detecting spectral shapes, because of its invariance under linear transformation of the data. That is, if you change the spectra by a gain (multiplicative factor) or by an additive factor, the correlation between X and Y remains unchanged. Thus, two curves that have an identical shape, but a different magnitude and offset, will still have a correlation of 1 for the SCM method. Furthermore, the method is able to detect anti-correlated objects, in contrast to SAM.

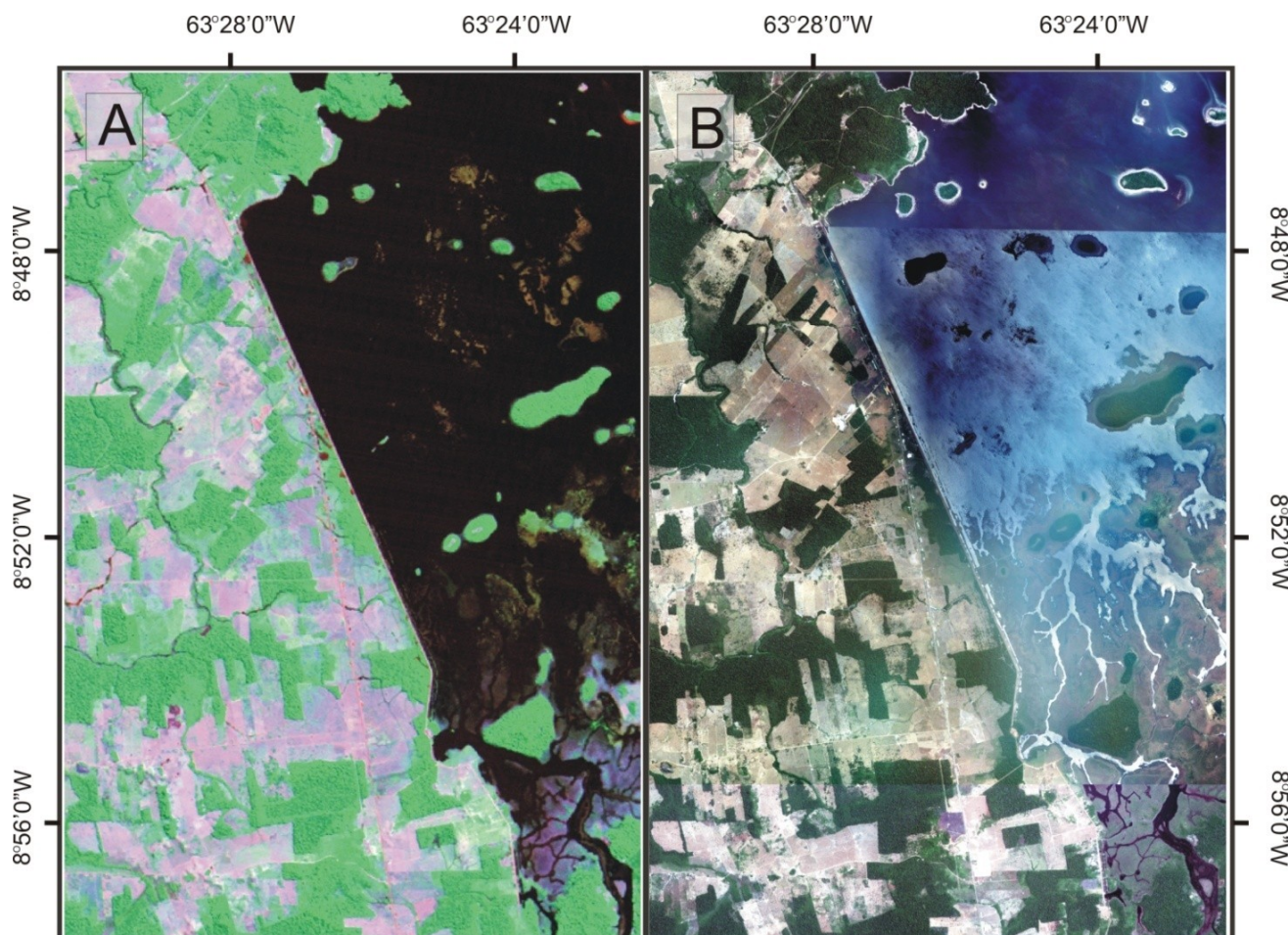
3.5. Accuracy Analysis

The classification obtained by the proposed method was compared to a classification by visual interpretation of Landsat-TM images on 15 July 2009 (Figure 4a). In addition, high-resolution images from Google Earth (Figure 4b) and fieldworks were used to assist in visual classification. The accuracy assessment used were the kappa coefficient and overall accuracy [47,48]. The overall accuracy is calculated by summing the number of pixels classified correctly and dividing by the total number of pixels. The kappa coefficient (K) is an accuracy measure of the classification described by the following equation:

$$K = \frac{m \sum_{i=1}^r s_{ii} - \sum_{i=1}^r s_{i+} s_{+i}}{m^2 - \sum_{i=1}^r s_{i+} s_{+i}} \tag{4}$$

where “*r*” is the number of rows in the error matrix, “*s_{ii}*” is the number of observation on row “*i*” and column “*i*”, “*s_{i+}*” and “*s_{+i}*” are thus the marginal totals on row “*i*” and column “*i*”, respectively, and “*m*” is the total number of observations.

Figure 4. (A) TM/Landsat-5 image on 15 July 2009, color composite 345 (RGB) and (B) high-resolution imagery archives from Google Earth.



3.6. Comparison with Other Traditional Methods

Radar imaging systems are based on backscattering from land cover, which generates a textural pattern characterized by different proportions of dark and light pixels, which prevent the direct use of classical techniques applicable to optical images. Thus, SAR images have specific characteristics that are quite different from optical remote sensing, depending on the scatter of ground objects and textural patterns, which vary with different targets. Normally, the traditional procedures for the classification of radar images are preceded by a step of filtering or texture analysis. Therefore, several texture descriptors have been adopted for SAR image classification.

A comparison of the proposed method should consider other methods that have univariate data as the input and multivariate data as the output, which generates multi-channels of textural attributes to describe a particular pixel. Thus, the multi-channel filtering approach decomposes the image into a number of filtered images, each of which contains intensity variations over a frequency and orientation [49,50]. In this approach, textural classification depends profoundly on the appropriate selection of the most promising attributes.

Thus, the proposed method is compared with traditional methods: the gray-level co-occurrence matrix (GLCM) and Gabor filters. The multi-channel methods allow the use of spectral classifiers (e.g., SCM and SAM) from a single image. In these studies, the local spectrum is established through features that are obtained by filtering the input image with a set of textural operators.

3.6.1. Gray-Level Co-Occurrence Matrices

The gray level co-occurrence matrix (GLCM) [51,52] is a traditional method for texture analysis based on second-order statistics, and its descriptors are the most commonly used for texture classification in a number of applications, for example, biomedical [53–55], textile industry [56,57], papermaking industry [58], and radar image processing [59,60], among others. The co-occurrence probabilities “ $C_{(i,j)}$ ” describe the relative frequencies of all pairwise combinations of grey levels (i,j) in the spatial window given an interpixel distance “ d ” and a specified orientation “ θ ”:

$$C_{ij} = \frac{P_{ij}}{\sum_{i,j=1}^G P_{ij}} \quad (5)$$

where P_{ij} represents the number of occurrence of grey levels pair (i,j), and G is the quantized number of grey levels. Co-occurrence matrix is a bi-dimensional histogram of the number of times that pairs of grey levels occur in a given spatial relationship [61].

Therefore, a singular GLCM is required for each parameter combination (d ; θ ; G ; window size). Thus, many studies have focused on the extraction of the optimal values for the different parameters of the GLCM. Usually, interpixel distances is short (1 or 2) when applied to remotely-sensed imagery [62–67]. Direction is especially important when there is anisotropy behavior; in this case, these are advocated individual orientations (0° , 45° , 90° , and 135°). However, the usual approach for remote sensing imagery is to combine multiple directions considering a mean [68]. The optimal grey-level quantization combines the acceleration of the statistical calculations, reduced noise and less loss of information. Typically, the most widely used quantization levels are 8, 16 and 32 [62,64,68,69].

A co-occurrence window width is an important parameter for classification purposes, relating to the target dimension in the studied image [70,71]. Each environment has its own optimal scale that may be different from image to image because of the noise or image orientation [72]. The window size should not take insufficient spatial information or the overlapping of two types of land cover classes [73]. Normally, the narrower windows size shows better results, mostly because larger window sizes cause problems at the boundaries between the classes [74,75]. However, Karathanassi *et al.* [70] using co-occurrence matrices in the panchromatic remote sensing images from the Satellite Pour l'Observation de la Terre (SPOT) sensor, have proven it to be more appropriate to use large window sizes (31×31 , 41×41 and 51×51). Dell'Acqua and Gamba [63] use multiple scale co-occurrence textural features to discriminate among different urban environments in SAR images. A method for determining the optimal window size is given by the smallest value of the coefficient of variation that starts to have a stable value [76].

Originally, 14 statistical parameters were extracted from GLCM [1]. However, these statistical descriptors show a redundancy of information, requiring a prior selection before classification in order to obtain measures that tend to be independent compared to other co-occurrence statistics [62,68,77–79]. According to Clausi and Zhao [80], five features are most used in practice: contrast, correlation, dissimilarity, entropy and uniformity. Baraldi and Parmiggiani [77] considered energy and contrast as the most useful for discriminating different textural patterns. The homogeneity (or inverse difference moment) and contrast have strong negative correlation, as well as entropy and energy [77]. However, the definition of texture features depends on the type of target investigated. For example, the best texture features for oil spill monitoring are contrast, correlation, dissimilarity and variance [81], while for urban land cover classification, they are angular second moment, contrast, homogeneity and entropy [82].

In this paper, we used a “*d*” value equal to one, a single horizontal direction, a “*G*” value equal to 16 and a window size of 11 pixels. The choice of the last two parameters was to be compatible with the proposed method (PDC). Furthermore, the classification can use a number of possible combinations among the textural descriptors. The problem is to choose the best combination of variables to obtain a classification with the lowest error. In this work, a technique of sequential search was adopted to select the best set of textural descriptors. The sequential search method aims to maximize the textural-descriptor prediction while employing the smallest number of combination. The method starts with a classification including all textural descriptors, and the calculation of its respective kappa index, in relation to manual classification. In the next step, the set of descriptors is subdivided into new subsets with one variable less, performing new classifications. For example, a model with five variables is subdivided into five new subsets with four variables. The greatest kappa index determines the best model, which is again subdivided eliminating a textural descriptor. The procedure continues, eliminating descriptors, until there is an improvement in predictive accuracy. The process stops, if the kappa index of the best model of *n*-elements was less than the best model of *n* – 1 elements. This procedure was used for the combinations of the seven main GLCM descriptors: dissimilarity (Dis), contrast (Cont), entropy (En), variance (Var), second-moment (SM), homogeneity (Hom), and correlation (Cor).

3.6.2. Gabor Filters

A Gabor function is a Gaussian modulated complex sinusoid in the spatial domain, which is widely applied to image processing, computer vision and pattern recognition [83,84]. Gabor filter formulation represented as a two-dimensional impulse response is described as [85–87]:

$$G(x, y; \theta, \lambda, \sigma_x, \gamma) = \frac{1}{2\pi\sigma_x\sigma_y} \exp\left\{-0.5\left[\frac{R_1^2}{\sigma_x^2} + \frac{R_2^2}{\sigma_y^2}\right]\right\} * \cos\left[\frac{2\pi R_1}{\lambda} + \psi\right] \quad (6)$$

where

$$R_1 = x \cos\theta + y \sin\theta \quad (7)$$

$$R_2 = -x \sin\theta + y \cos\theta \quad (8)$$

$$\sigma_y = \frac{\sigma_x}{\gamma} \quad (9)$$

where the arguments “ x ” and “ y ” are the position in the window filter; “ θ ” specifies the orientation of the normal to the parallel stripes of the Gabor function; “ λ ” specifies the wavelength that is given in pixels; “ σ_x ” and “ σ_y ” specify the standard deviations of the Gaussian factors determining the size of the receptive field; “ γ ” is the spatial aspect ratio that determines the ellipticity of the receptive field; and “ ψ ” is the phase offset of the cosine factor of the Gabor function expressed in degrees. Thus, the Gabor filter depends on a number of parameters that need to be set appropriately.

The spatial frequency bandwidth (σ/λ), considering the value of 0.56, is widely used in the textural analysis [86–89]. In this case, the parameters, σ and λ , are not independent and only one of them is a free parameter. In this paper, we used $\sigma/\lambda = 0.56$, $\gamma = 1$ and $\psi = 0$.

A multi-channel filtering approach can be implemented, where an image is filtered by a set of suitable Gabor filters at different orientations and spatial frequencies, resulting in a filter bank design used for analysis, classification or segmentation [90,91]. Several authors proposed filter bank designs for various applications [50,92–96]. In this paper, we use a filter bank, with four values of orientation (0° , 45° , 90° and 135°) and three spatial frequencies ($0.5\sqrt{2}$, $1\sqrt{2}$, and $2\sqrt{2}$ cycles per image-width) [50]. Thus, twelve even-symmetric Gabor filters are used in the study. The values of spatial frequency (f) are determined considering the following equation [50]:

$$f = \frac{Nc\sqrt{2}}{4} \quad (10)$$

where, “ Nc ” varies in a value range expressed as a power of two (between two and the window size). Normally, the window size coincides with a value of a power of two. In this paper, we adopted a window size equal to 11, but a maximum value of Nc equal to 8 (the closest value of the window size) that establishes a wavelength of 11.31, 5.66 and 2.83 ppc. These wavelength values were also used by [92,97].

4. Experimental Results

4.1. Probability Density Components

For the use of the PDCA method in ALOS-PALSAR images, we considered a window size of 11×11 and the number of bins to be 16. Figure 5 shows the 3D cube image with a cube face formed by an RGB color composite (1PDC/8PDC/16PDC).

Figure 5. 3D image cube composed of probability density components (PDCs), where a cube face is an RGB color composition (1PDC, 8PDC and 16PDC).

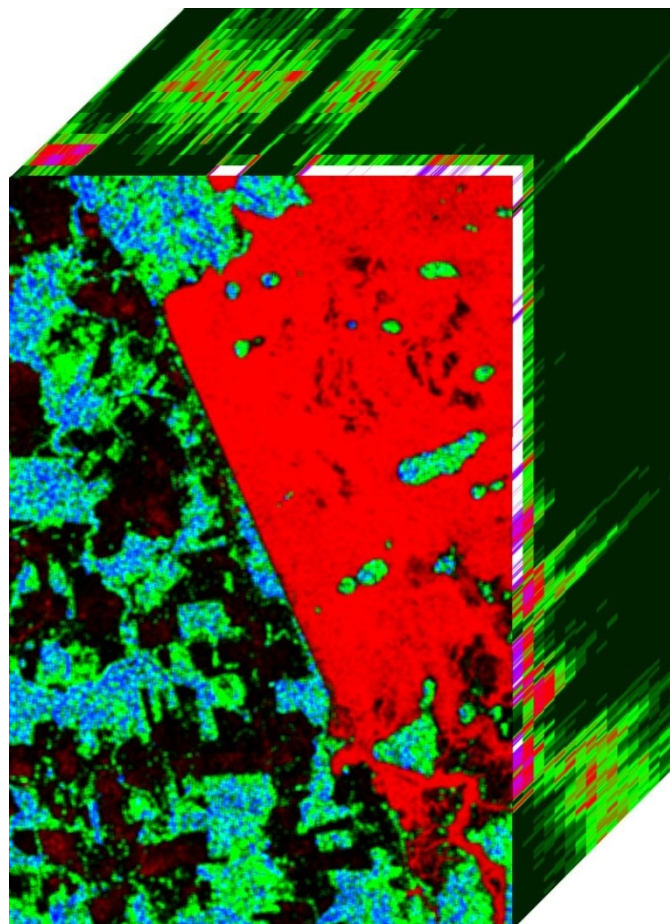


Figure 6 shows the probability density components relating to the 16 bins. The first component shows high intensity areas related to water bodies. The other bands reflect a gradation that shows the distributions of the backscattered field amplitude for the different classes. Thus, the images show the increased radar reflectivities, where the first bands highlight the pasture and agricultural area, while the latter bands shows the secondary vegetation and forest.

The PDC images were subjected to NAPC transformation. PDC-NAPCs show an increasing noise fraction from the first toward the last. The signal fraction is grouped into the first five components (Figure 7A–E), while the remaining bands represent the noise components (Figure 7F–G). The high performance of the NAPC transform in ordering the components by image “quality” is readily apparent in Figure 7.

Figure 6. Probability density components from a window size of 11×11 and 16 bins: (A) 1PDC; (B) 2PDC; (C) 3PDC; (D) 4PDC; (E) 5PDC; (F) 6PDC; (G) 7PDC; (H) 8PDC; (I) 9PDC; (J) 10PDC; (K) 11PDC; (L) 12PDC; (M) 13PDC; (N) 14PDC; (O) 15PDC; and (P) 16PDC.

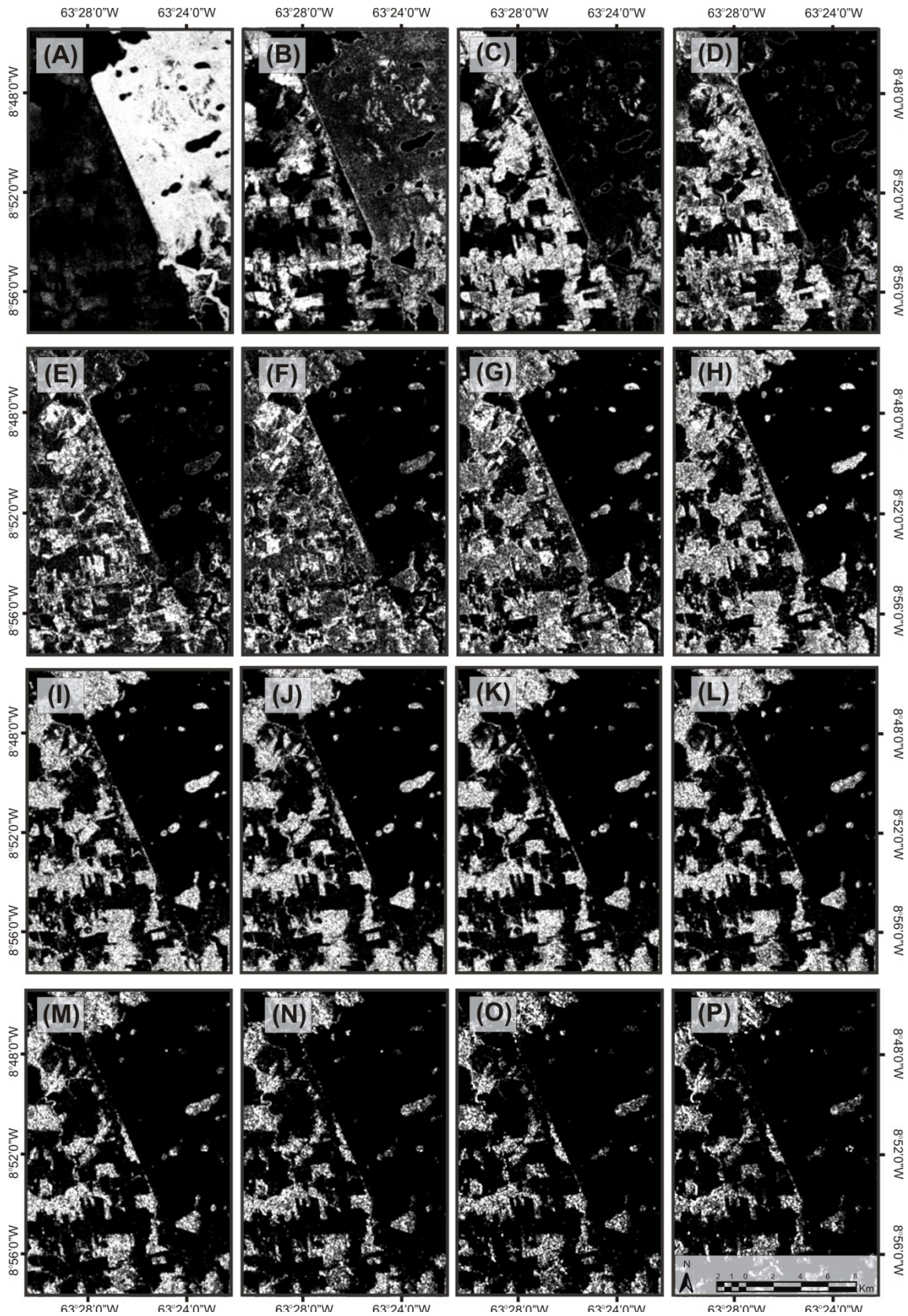
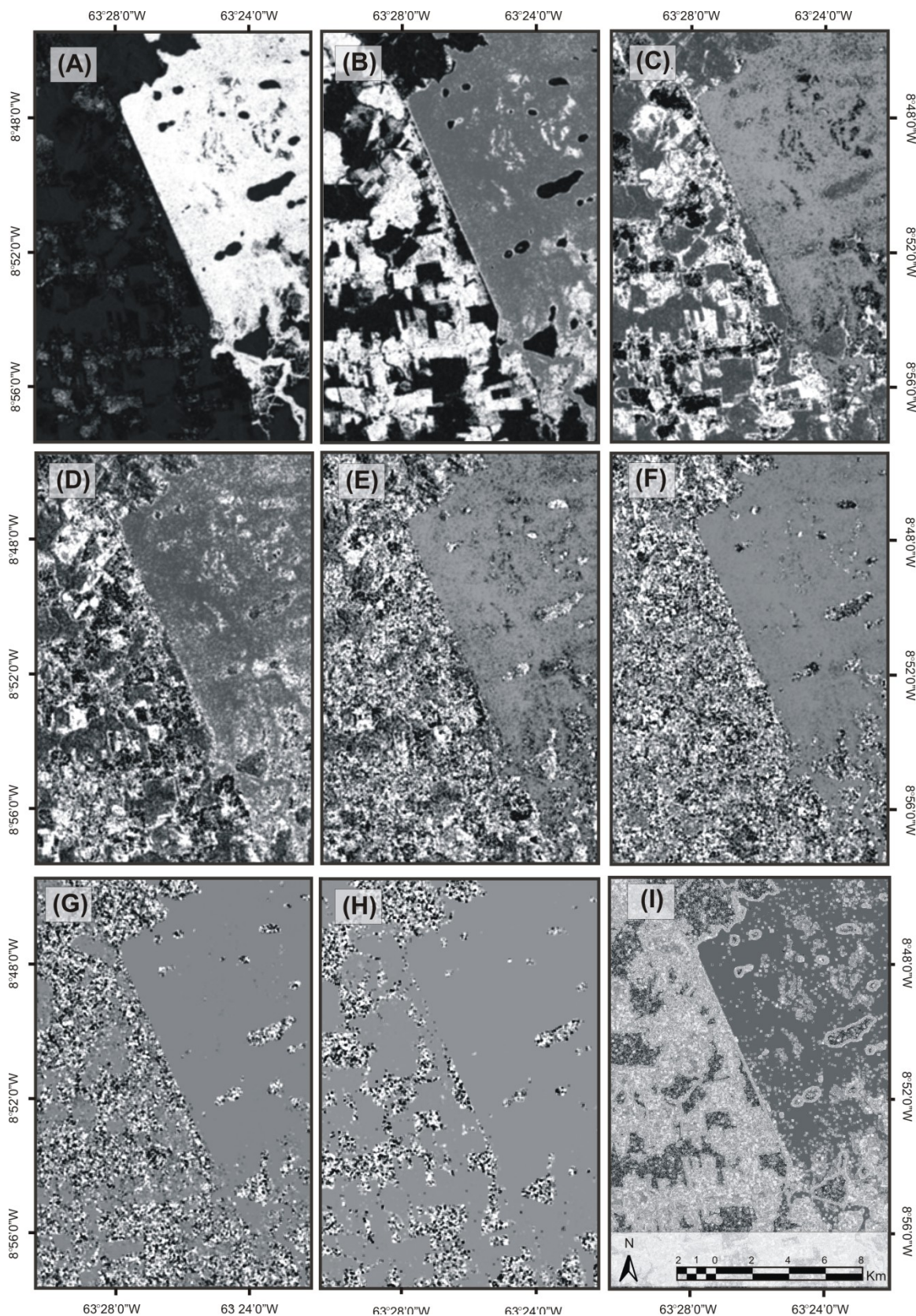
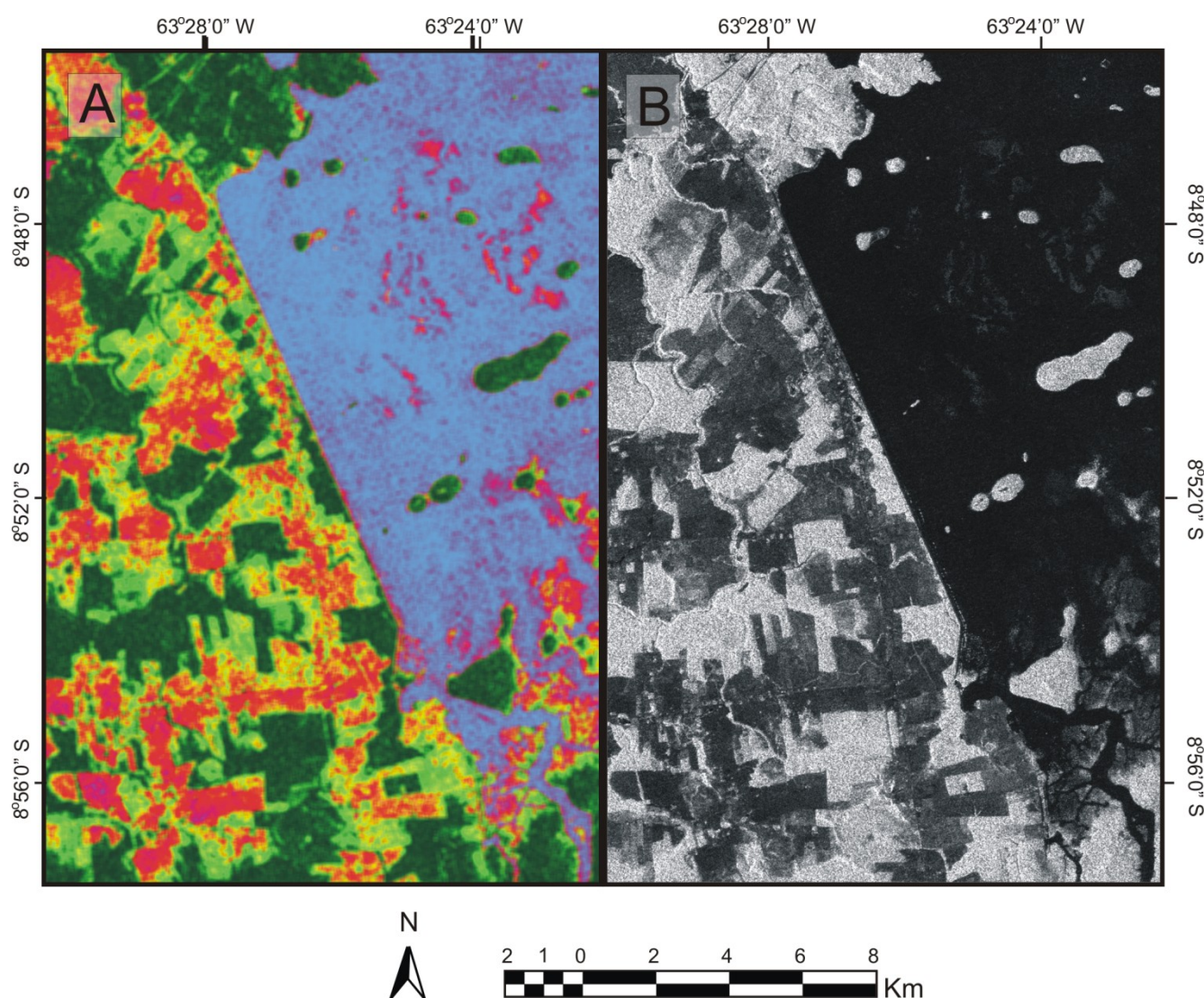


Figure 7. Noise-adjusted principal component (NAPC) transform of the probability density components: (A) 1PDC-NAPC; (B) 2PDC-NAPC; (C) 3PDC-NAPC; (D) 4PDC-NAPC; (E) 5PDC-NAPC; (F) 6PDC-NAPC; (G) 14PDC-NAPC; (H) 15PDC-NAPC; and (I) 16PDC-NAPC.



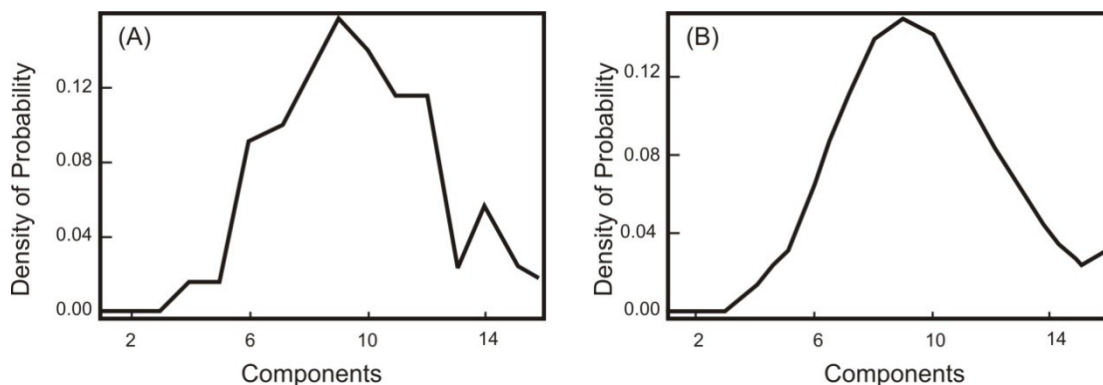
The color composites considering the first NAPCs enhance the reservoir, land use areas and forest (Figure 8A). This simple procedure already provides a significant contrast between the targets, evidencing the different patterns from original radar image (Figure 8B). Moreover, NAPC signal components eliminate the granular aspect of the radar image. The NAPC application performs an optimal smoothing in the spectral domain without affecting the spatial resolution. Thus, the deconvolution of a single image in various components with different spatial frequencies and the subsequent information concentration by NAPC transformation enable one to obtain a high quality and colorful result that differentiates it from all other methods developed for radar images.

Figure 8. (A) RGB Color Composite: 2PDC-NAPC (red), 3PDC-NAPC (green) and 1PDC-NAPC (blue); and (B) HV PALSAR-ALOS image.



In order to eliminate noisy features in the probability density curve, the inverse NAPC rotation was performed, considering the six signal components. This procedure allows an intense smoothing of the probability density curve, without serious signal degradation (Figure 9). The amount of noise reduction is dependent on the correlation among components.

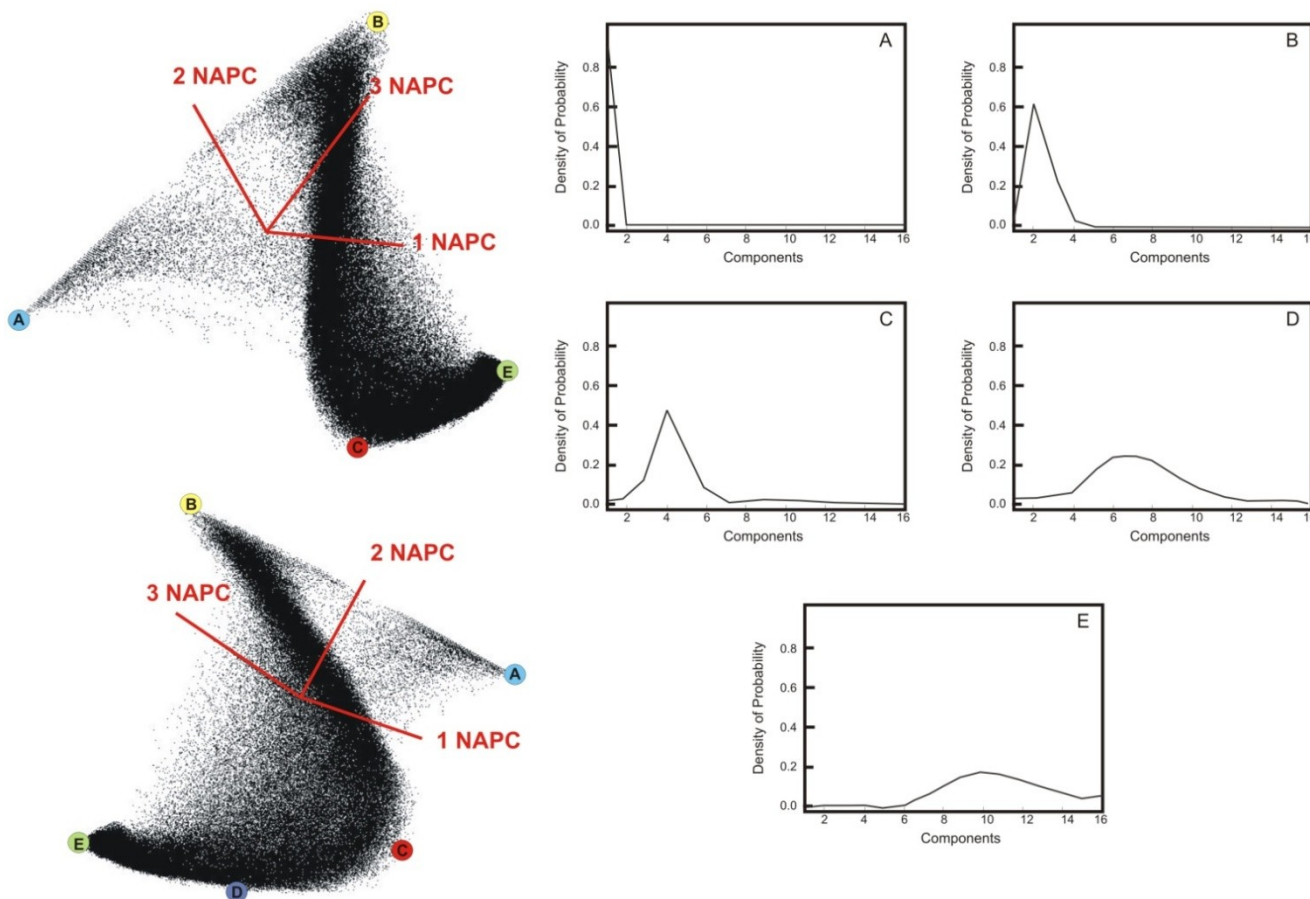
Figure 9. Noise treatment of the PDC by the use of inverse NAPC rotation: (A) original data and (B) result after denoise processing.



4.2. Classification of the Probability Density Components

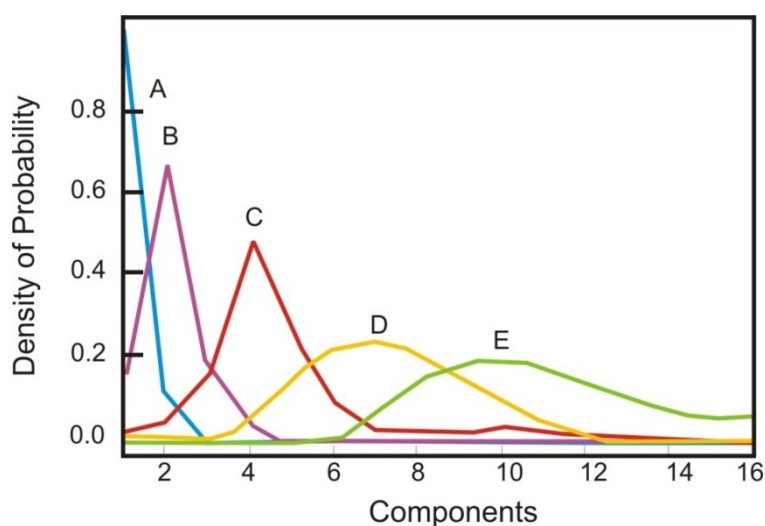
The endmembers were identified by visualization in the n-dimensional scatter plot of the first three NAPCs. The point distribution shows a configuration in the shape of an “S” (Figure 10). The endmembers are positioned in the inflection and extremes. The five endmember have an arrangement with a gradual increase in the values of the bins and the dispersion of the data, which corresponds to a gradient from a specular reflector (water, bare soil, margin of the reservoir) to a diffuse reflector (secondary forest, forest).

Figure 10. Endmember identification using the n-dimensional scatter plot.



The water curve has a frequency accumulated in the first bin, because when the pulse hits the flat surface, most of the energy is directed outwards away from the surface at a right angle away from the receiver; so, little energy is recorded (Figure 11, Curve “A”). The spectra with high frequency in the second bin represent exposed soil present on the margins of reservoirs and degraded pastures (Figure 11, Curve “B”). Pasture and agricultural areas show the highest density of probability in Bin 4 (Figure 11, Curve “C”). The secondary forest as a result of human activity disruption, such as logging and abandoned pastures, show a spectrum with higher amplitude and the highest probability density for Bin 7 (Figure 11—Curve “D”). The forest curve has the highest dispersion. In this environment, the radar pulse is scattered at different angles because of the contribution of backscattering from the various structures, such as stems, leaves, trunks and branches (Figure 11, Curve “E”).

Figure 11. Probability density signatures in the study area (A, B, C, D and E curves).



The images were classified using the spectral measures: SCM and Euclidian distance. Classes related to B and C endmembers represent the same group, when compared with the optical images (Figure 4). Thus, the final classification received only four classes that are most significant to the studied area (Figure 12A). The classes from the proposed method are homogeneous without anomalous points and do not require the use of post-classification methods, which are commonly found in radar image classification. These classes have a high correlation with the features highlighted in the RGB color composite of PDC-NAPCs (Figure 8).

The accuracy indices are slightly higher for the SCM classification (kappa coefficient = 0.8137 and overall accuracy = 87.08%) in relation to the Minimum Distance (kappa coefficient = 0.8035 and overall accuracy = 86.4302%). Therefore, the resulting image classification shows great similarity to visual image interpretation (Figure 12). Table 1 shows the confusion matrix for the SCM classification. The largest error occurs in the class of secondary forest and disturbed forest, because of its heterogeneous behavior. In this class, a wide variety of anthropogenic disturbances is agglutinated, such as selective logging by hand, silvicultural measures that kill non-commercial species in support of trade, and abandoned pastures, among others. In addition, secondary growth includes a wide distribution of weedy herbaceous plants and fast-growing vines, forming a dense canopy of forest that varies with age. All these variations hinder the accurate detection of this class.

Figure 12. Classified maps using (A) the Spectral Correlation Mapper from the probability density curves; and (B) visual interpretation from high-resolution optical images.

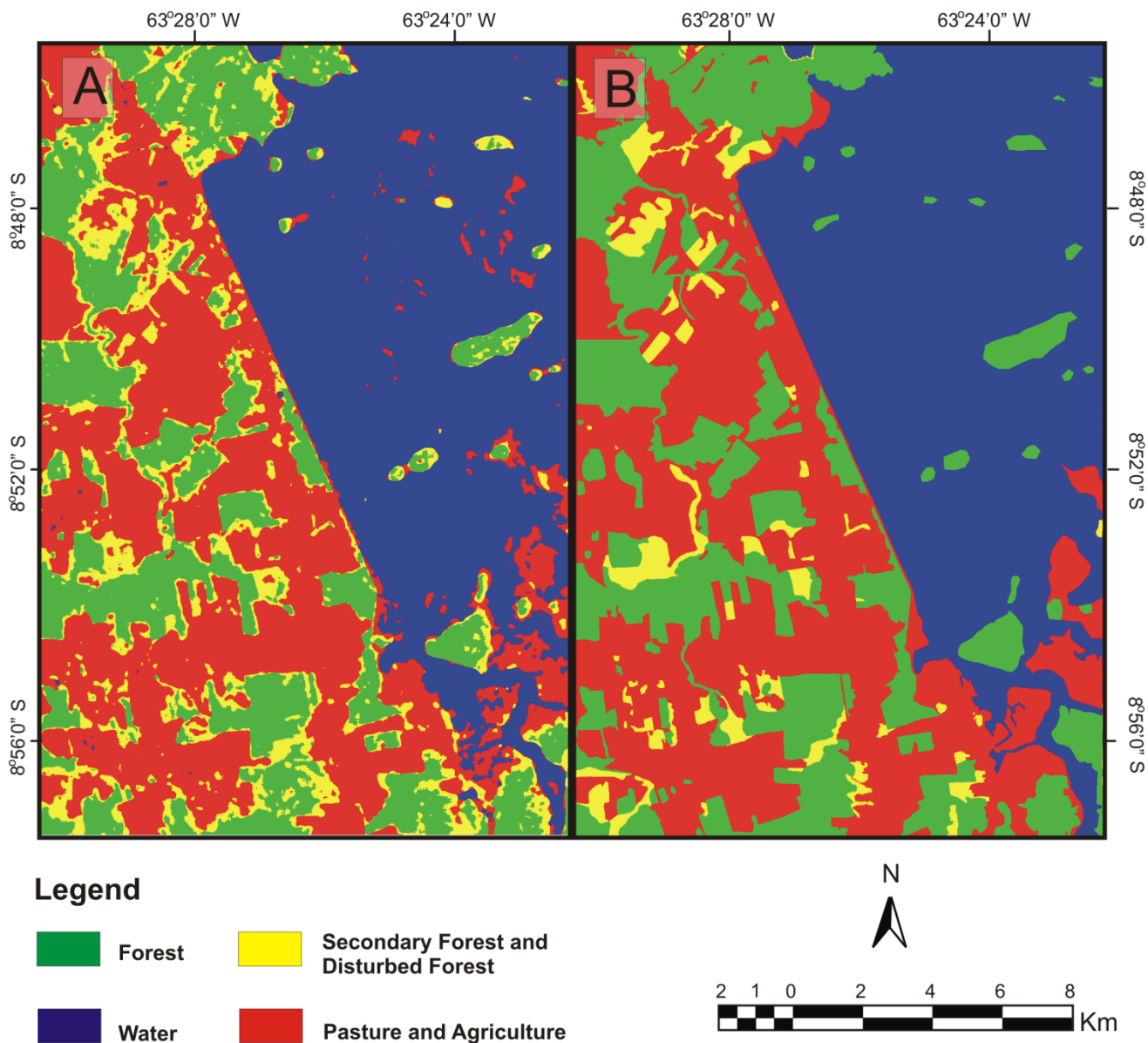


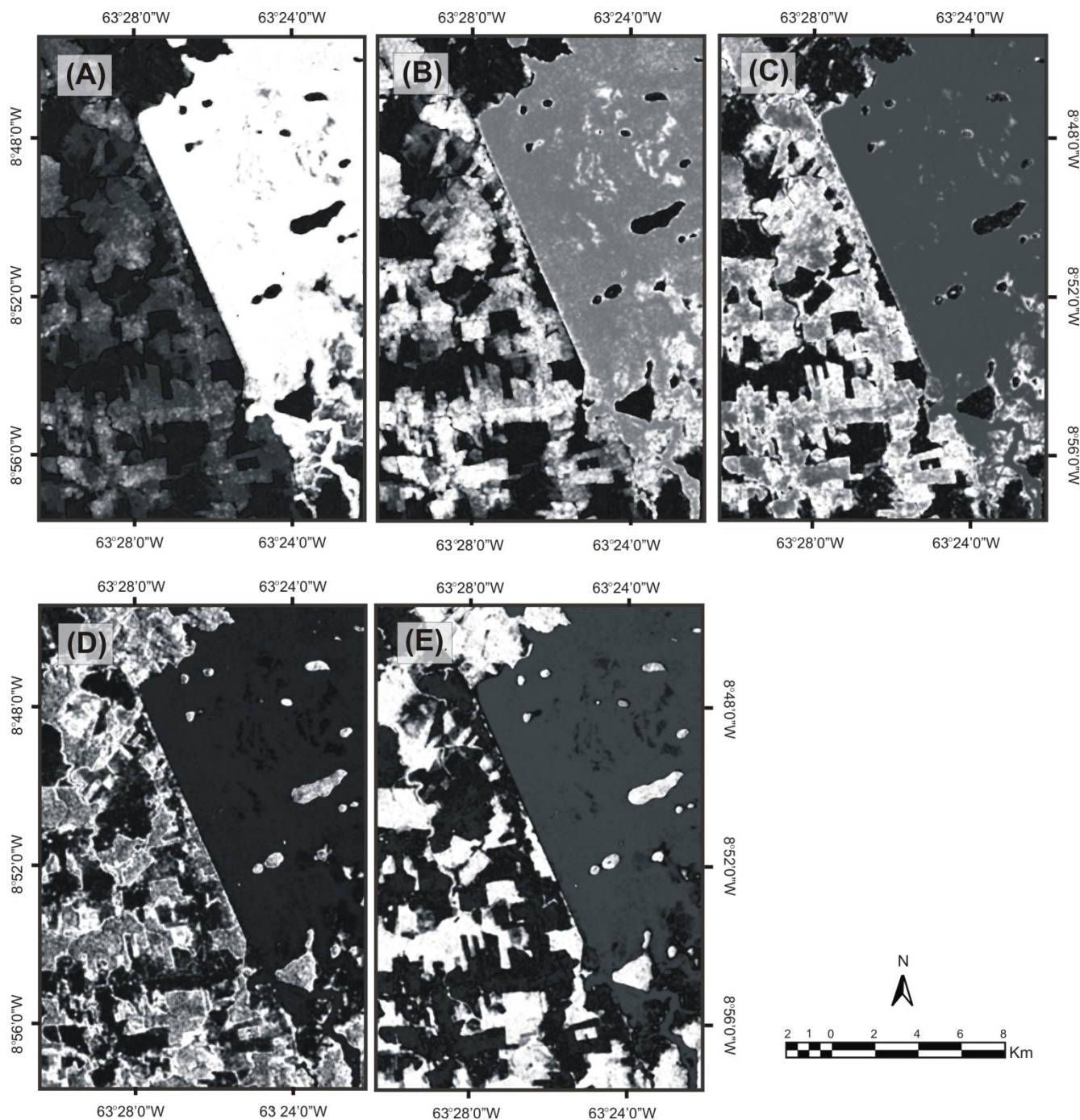
Table 1. Confusion or error matrix for four classes.

Image Classification	Ground Truth (Percent)			
	Pasture and Agriculture	Secondary Forest	Forest	Water
Pasture and agriculture	87.33	19.43	4.78	3.38
Secondary Forest	8.61	66.78	18.54	0.45
Forest	1.27	13.38	75.62	0.14
Water	2.79	0.42	1.06	96.04
Total	100.00	100.00	100.00	100.00

Furthermore, along the boundaries between the pasture and forest classes, the presence of narrow strip of secondary forest and disturbed forest was erroneously detected. This error is due to the interference of two classes in the moving window, generating an intermediate curve similar to secondary forest.

Figure 13 shows the rule images of the SCM classification. These images show the probability that a pixel corresponds to a specific endmember. In the case of the SCM classifier, the higher intensity corresponds to a greater probability of the pixel belonging to the class. Figure 13A shows the rule image from probability density curve “A”, which highlights the reservoir area with the presence of small islands. Figure 13B–D shows human activity areas with a gradual increase of biomass and dispersion. Figure 13E highlights areas of forest present in the radar image.

Figure 13. Rule images of the Spectral Correlation Mapper (SCM) method, considering the endmembers of Figure 10: (A) Curve A; (B) Curve B; (C) Curve C; (D) Curve D; and (E) Curve E.



4.3. Results of the Comparison with Other Traditional Methods

The textural classifications (GLCM and Gabor Filter) were tested with the same window size (11 × 11), endmembers and spectral classifiers (similarity and distance measures) in order to limit the comparison to only the textural descriptors. The comparison among the methods considered the accuracy indices (kappa coefficient and the overall coefficient) between the textural classification and the visual interpretation from high-resolution optical images.

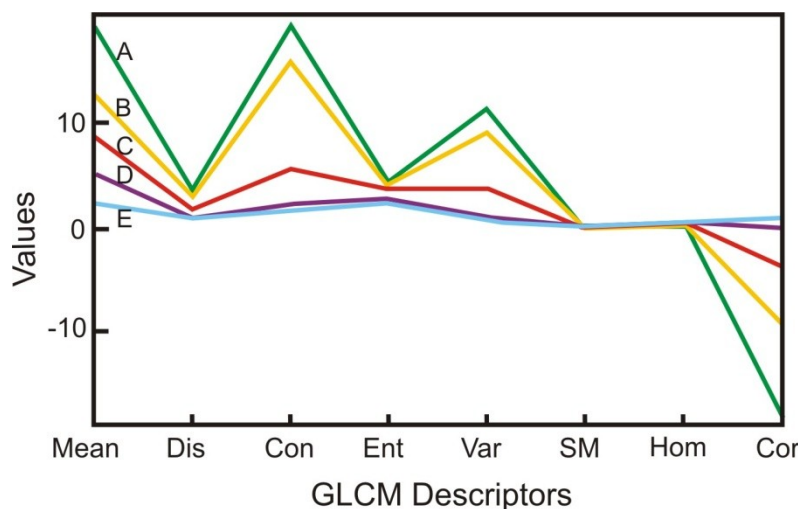
4.3.1. Gray-Level Co-Occurrence Matrices

Co-occurrence images present a high correlation, particularly with respect to Dis and Con (Table 2). The SCM classification shows bad results because of high similarity among the endmembers. Figure 14 shows the endmember curves, containing all the GLCM-descriptor values. These endmembers display the same shape of curves, differing only in the intensity values. Thus, SCM classification using all descriptors obtained lower values for the kappa coefficient (0.4099) and overall accuracy (55.0313%). In contrast, the minimum distance classification from all descriptors showed better results (kappa coefficient = 0.6438 and overall accuracy = 74.6121%).

Table 2. Correlation matrix among the gray-level co-occurrence matrix (GLCM) descriptors. Dis, dissimilarity; Con, contrast; Ent, entropy; Var, variance; SM, second moment; Hom, homogeneity; Cor, correlation.

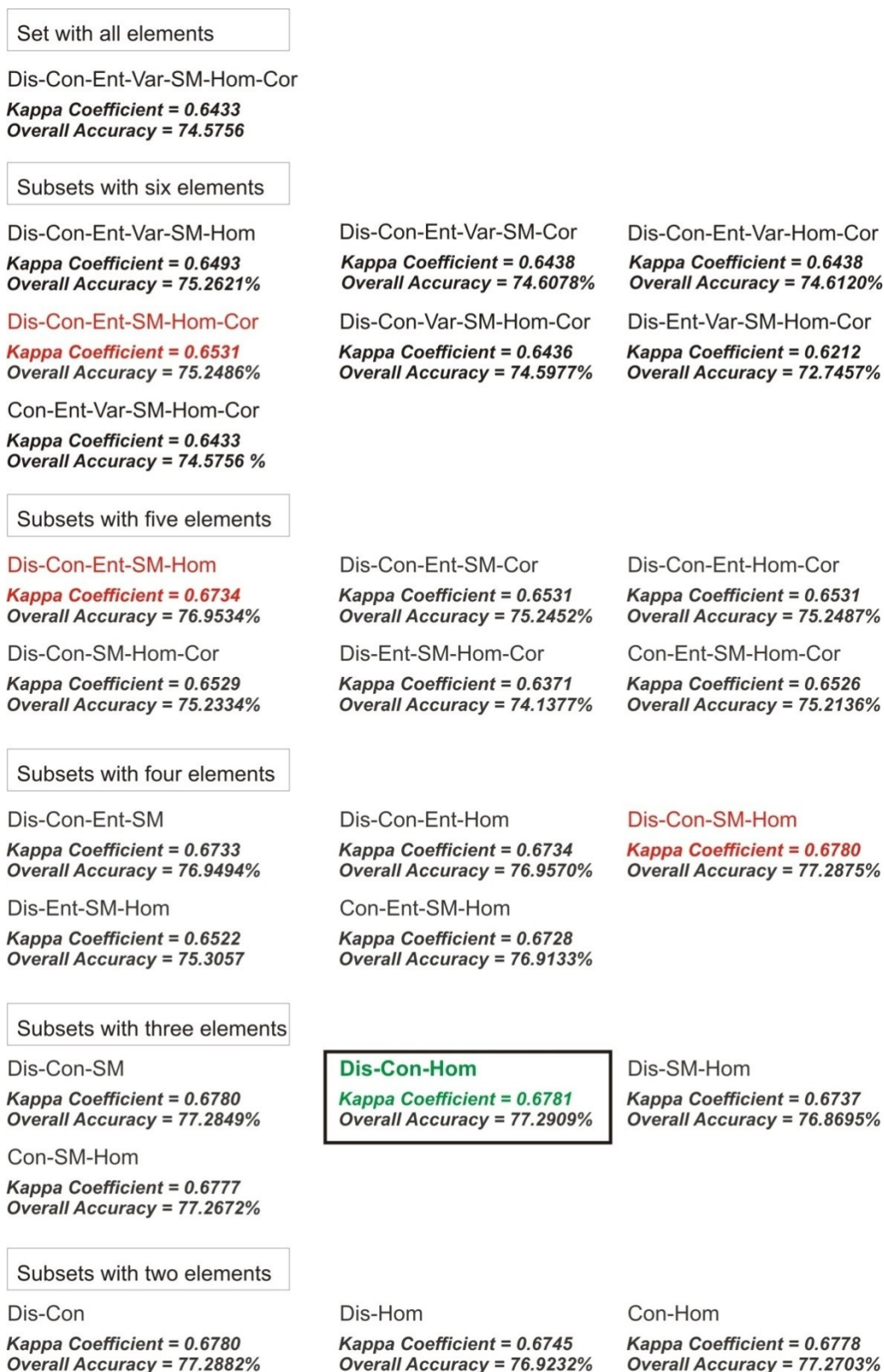
	Dis	Con	Ent	Var	SM	Hom	Cor
Dis	1.00	0.97	0.89	0.85	-0.76	-0.84	-0.88
Con	0.97	1.00	0.78	0.86	-0.66	-0.79	-0.83
Ent	0.89	0.78	1.00	0.74	-0.80	-0.73	-0.81
Var	0.85	0.86	0.74	1.00	-0.63	-0.71	-0.64
SM	-0.76	-0.66	-0.80	-0.63	1.00	0.92	0.77
Hom	-0.84	-0.79	-0.73	-0.71	0.92	1.00	0.83
Cor	-0.88	-0.83	-0.81	-0.64	0.77	0.83	1.00

Figure 14. GLCM-descriptor signatures for the study area: (A) Curve A; (B) Curve B; (C) Curve C; (D) Curve D; and (E) Curve E.



The sequential search method for the selection of the best textural descriptors was applied to the classified images by Euclidian distance. Figure 15 schematically shows the subsets of descriptors and their respective accuracy indices.

Figure 15. Sequential search scheme for the selection of the best GLCM descriptors.



In the scheme shown in Figure 15, the best subset of each stage (highest value of the kappa coefficient) is marked in red. The best subset of a stage is subdivided into subsets with one descriptor less in the next stage, *i.e.*, eliminating the descriptor that does not belong to the winner subset. The kappa coefficients have changed little among the different subsets, ranging between 0.64 and 0.67. This is due to the high correlation among the GLCM descriptors. The best configuration (Kappa Coefficient = 0.6781 and Overall Accuracy = 77.29%) was composed of the following descriptors: dissimilarity (Dis), contrast (Cont), and homogeneity (Hom). These accuracy values were lower than the PDC-NAPC method.

4.3.2. Gabor Filter

The classifications from all spatial frequencies ($0.5\sqrt{2}$, $1\sqrt{2}$, and $2\sqrt{2}$ cycles per image-width) presented results with low accuracy values. The classification using the SCM method has accuracy indices that are extremely low, demonstrating its inadequacy in dealing with this type of data. However, the Minimum Distance method shows reasonable results (kappa coefficient = 0.6467 and Overall Accuracy = 75.8391%).

The successive elimination of higher frequencies caused an improvement in classification accuracy. As might be expected, the higher frequency images highlighted the edge detection, but contributed little to distinguishing the land-cover classes. The higher the filter frequency, the greater the interference of impulse noise in the image [92]. Therefore, image classification using the two lowest spatial frequencies presented an improved in the Kappa Coefficient (0.6822) and Overall Accuracy (77.9726%). The best result was obtained using only the images of the lowest spatial frequency (Kappa coefficient = 0.7234 and Overall Accuracy = 80.6727%). These accuracy values were higher than the best result of the GLCM method; but remained lower than the PDC-NAPC method.

4.4. Program

The methods discussed are available in software developed in the C++ language (<http://lsie.unb.br/abilio>). The main functions of the program are organized in the main window interface, which contains the image input boxes, method modules and image display. The program reads general raster data stored as an interleaved binary stream of bytes in band sequential format (BSQ). Each image is accompanied by a header file in American Standard Code for Information Interchange (ASCII) containing information to read the data file, such as sample numbers, line numbers, bands, the interleave code (BSQ) and the data type (byte, signed and unsigned integer, long integer, floating point, 64-bit integer, unsigned 64-bit integer). This configuration, combining the image and header file, allows for versatility in the use of different image formats. When the user tries to open an image without the header file, an interface requesting the necessary information about the input image structure automatically appears.

The software is divided into three modules: (1) the PDCA method; (2) forward and inverse transformation NAPC; and (3) the SCM classifier. The PDCA method considers as input the following parameters: a single radar image, the number of bins representing the number of components and the size of the moving window. The PDCA generates the following output data: an image composed of all components and a single image in grayscale relating to bins determined by the user. The forward NAPC transformation considers as input the PDCs and the number of neighborhoods to be used in

calculating the matrix of noise. The inverse transformation NAPC considers as input the signal components of the NAPC and the eigenvectors matrix of the forward NAPC rotation. Finally, the SCM method takes as input data the endmembers and the components after the noise removal.

All inputs and results are shown in the file list, so it is possible to visualize them by choosing “gray scale” or “RGB” composite. The display interface provides basic functions for images visualization such as zoom areas and pixel values. Moreover, the results (output files) can be read from other viewers of binary images.

5. Discussions

In examining SAR data, a crucial issue is the challenge of developing accurate models for the statistics of pixel intensities, with the purpose of classifying or filtering. In this article, the main objective was to show a new algorithm that improves the SAR image classification. The algorithm combines different methods; some procedures have already been applied in radar images (PDF and filters by moving-window) and others from methods for hyperspectral images processing (MNF, pixel purity index and SCM) are still unused. One of the main innovations compared to already published strategies is the elaboration of the probability density curves for each image pixel using a moving window approach, which generates multi-components that minimize noise and enable the application of spectral classification techniques. Unlike other moving-window filters [1–7], the new approach generates several output images referring to different frequencies from a single input image. This approach is similar to multi-channel filtering approach from GLCM and Gabor filter. Besides, the moving-window procedure establishes a spatial pattern in the elaboration of the probability density curves, favoring the comparison and classification. Normally, in other studies, PDF estimation considers a large number of samples [9,16]; in this new approach, smaller datasets are used, which decrease the mixing between classes and suggest the good stability of the probability density curves.

The proposed algorithm has two free parameters, which must be adjusted to obtain a histogram with a good quality sample distribution. In the present study, we used a window size of 11×11 pixels that generates 121 samples that are distributed in 16 bins. Despite the good results shown by sample distribution, new studies may test other combinations in order to have a gain in performance. Since the radar image is converted to the PDC components, it is not possible to obtain an inverse transform.

NAPC transformation is applied in the PDC components in order to minimize the noise of the probability density curves. This procedure is very different from the conventional methods of noise removal in radar images, which operates on a single image. Therefore, this new approach using multi-components has no similarity with other methods applied to radar data, but is compatible with the procedures used in hyperspectral images [98–101], aerial gamma-ray surveys [33,34,102,103] and time-series data [35–37]. The key to success is in the reconstruction of a valid signal and the attenuation of noise from the PDC components. Thus, this new data configuration allows the use of several methods of digital image processing used for others data types.

We did a test on a well-known and representative area of the Amazon Forest, where the model achieves the accurate detection of targets. Forest mapping using radar data is particularly important in the tropics, where optical sensors are often constrained by the presence of haze, smoke or clouds. However,

the proposed method should be further tested in other environments in order to evaluate its performance for different targets. For this, the algorithm is in free software for those who want to test it.

The PDCA method was compared with the GLCM and Gabor methods, widely used in the SAR image classification and texture analysis. These methods present various free variables that provide a wide variety of results. In this study, different combinations of descriptors were tested in order to obtain better classification accuracy. The best combination of GLCM descriptors was composed of dissimilarity, contrast, and homogeneity. However, the accuracy values among the best descriptor set and other subsets are statistically very close, because of the high multicollinearity of GLCM images. The best descriptors from Gabor filter images are the lower spatial frequency ($0.5\sqrt{2}$ cycles per image-width) in four orientations (0° , 45° , 90° and 135°).

A limitation of the proposed method is the classification on the boundaries of different classes. In these locations, the probability density curve displays a hybrid behavior of the two classes causing difficulty in classification. Future work will mainly cover the development of new algorithms for this specific problem. In addition, others radar bands or methods of noise elimination, endmember identification and classification can be tested.

6. Conclusions

The PDCA method is conceptually simple and effective in speckle filtering and allows a supervised classification from the probability density curves. The probability density curve describes a stationary condition, mainly after the noise elimination with the NAPC transform, which facilitates the classification. In this case, the spatial frequencies of the radar images are distributed in different images, which is an improvement to their representation, unlike other methods that are limited to only one output image. In this sense, the color composition of the PDC-NAPC signal components is an interesting enhancement technique highlighting the main surface targets and allowing for significant improvement of single image radar.

The PDCs can be treated similarly to the multispectral images from optical sensor systems or aerial gamma-ray surveys. Endmembers of probability density curves are identified using the n-dimensional scatter plot and the classification is accomplished through the SCM method. The probability distribution for the amplitude and intensity SAR data is far from being symmetric because of the Rayleigh distribution. However, in this study, the asymmetry attribute is a factor for endmember individualization. The method also does not have difficulties in identifying targets with strong returns from point scatters as well as targets with very low intensities and very small ranges. Thus, the method is suitable for discriminating different types of scattering. However, there are still several issues that can be investigated in future research in order to enhance and achieve better performance, such as the sensitivity analysis of free parameters, comparisons with other methods, and applications to other environments. All these factors are challenges for SAR image processing and the spectral-analysis algorithms extend the processing alternatives.

Acknowledgments

This study was funded through a project from Conselho Nacional de Desenvolvimento Científico e Tecnológico (CNPq). The authors are thankful for the financial support from a CNPq fellowship

(Osmar Abílio de Carvalho Júnior, Renato Fontes Guimarães and Roberto Arnaldo Trancoso Gomes). Special thanks are given to Financiadora de Estudos e Projetos (FINEP) for additional support.

Author Contributions

Osmar Abílio de Carvalho Júnior wrote the manuscript and was responsible for the research design, mathematical model, data preparation and analysis. Luz Marilda de Moraes Maciel and Ana Paula Ferreira de Carvalho provided some of the data, conducted the field-works and gave relevant technical support. Renato Fontes Guimarães and Roberto Arnaldo Trancoso Gomes supported the analysis and interpretation of the results. Nilton Correia da Silva and Cristiano Rosa Silva provided significant input to the numerical analysis, computational optimization and object-oriented programming. All of the authors contributed in editing and reviewing the manuscript.

Conflicts of Interest

The authors declare no conflict of interest.

References

1. Goodenough, D.G.; Guindon, B.; Teillet, P.M. Correction of Synthetic Aperture Radar and Multispectral Scanner Data Sets. In Proceedings of the Thirteenth International Symposium on Remote Sensing of Environment, Ann Arbor, MI, USA, 23–27 April 1979; Volume 2, pp. 259–270.
2. Henninger, D.L.; Carney, J.H. Shuttle Imaging Radar-A (SIR-A) Data as a Complement to Landsat Multispectral Scanner (MSS) Data. In Proceedings of the International Geoscience and Remote Sensing Symposium (IGARSS'83), San Francisco, CA, USA, 31 August–2 September 1983; pp. 7.1–7.7.
3. Lee, J.S. Digital image smoothing and the sigma filter. *Comput. Vis. Graph. Image Process.* **1983**, *24*, 255–269.
4. Lee, J.S. A simple speckle smoothing algorithm for synthetic aperture radar images. *IEEE Trans. Syst. Man Cybern.* **1983**, *13*, 85–89.
5. Lee, J.S.; Wen, J.-H.; Ainsworth, T.L.; Chen, H.-S.; Chen, A.J. Improved sigma filter for speckle filtering of SAR imagery. *IEEE Trans. Geosci. Remote. Sens.* **2009**, *47*, 2002–2013.
6. Lee, J.S. Digital image enhancement and noise filtering by use of local statistics. *IEEE Trans. Pattern Anal. Mach. Intell.* **1980**, *2*, 165–168.
7. Kuan, D.T.; Sawchuk, A.A.; Strand, T.C.; Chavel, P. Adaptive noise filtering for images with signal dependent noise. *IEEE Trans. Pattern Anal. Mach. Intell.* **1985**, *7*, 165–177.
8. Gao, G. Statistical modeling of SAR images: A survey. *Sensor* **2010**, *10*, 775–795.
9. Nezry, E.; Lopés, A.; Ducrot-Gambart, D.; Nezry, C.; Lee, J.S. Supervised classification of K-distributed SAR images of natural targets and probability of error estimation. *IEEE Trans. Geosci. Remote Sens.* **1996**, *34*, 1233–1242.
10. George, S.F. *The Detection of Nonfluctuating Targets in Log-Normal Clutter*; NRL Report 6796; Naval Research Laboratory: Washington, DC, USA, 1968.

11. Ulaby, F.T. Textural information in SAR images. *IEEE Trans. Geosci. Remote Sens.* **1986**, *24*, 235–245.
12. Tison, C.; Nicolas, J.M.; Tupin, F. Accuracy of Fisher Distributions and Log-Moment Estimation to Describe Histograms of High-Resolution SAR Images over Urban Areas. In Proceedings of 2003 IEEE International Geoscience and Remote Sensing Symposium, IGARSS'03, Toulouse, France, 21–25 July 2003; pp. 21–25.
13. Tison, C.; Nicolas, J.M.; Tupin, F.; Maitre, H. A new statistical model for Markovian classification of urban areas in high-resolution SAR images. *IEEE Trans. Geosci. Remote Sens.* **2004**, *42*, 2046–2057.
14. Oliver, C.; Quegan, S. *Understanding Synthetic Aperture Radar Images*; Artech House: Norwood, MA, USA, 1998.
15. Duda, R.O.; Hart, P.E.; Stork, D.G. *Pattern Classification*, 2nd ed.; Wiley: New York, NY, USA, 2001.
16. Moser, G.; Serpico, S.B.; Zerubia, J. Dictionary-based stochastic expectation maximization for SAR amplitude probability density function estimation. *IEEE Trans. Geosci. Remote Sens.* **2006**, *44*, 188–200.
17. Parzen, E. On estimation of probability density function and mode. *Signal Process.* **1962**, *33*, 267–281.
18. Bruzzone, L.; Marconcini, M.; Wegmuller, U.; Wiesmann, A. An advanced system for the automatic classification of multitemporal SAR images. *IEEE Trans. Geosci. Remote Sens.* **2004**, *42*, 1321–1334.
19. Mantero, P.; Moser, G.; Serpico, S.B. Partially supervised classification of remote sensing images through SVM-based probability density estimation. *IEEE Trans. Geosci. Remote Sens.* **2005**, *43*, 559–570.
20. Krylov, V.A.; Moser, G.; Serpico, S.B.; Zerubia, J. Enhanced dictionary-based SAR amplitude distribution estimation and its validation with very high-resolution data. *IEEE Geosci. Remote Sens. Lett.* **2011**, *8*, 148–152.
21. Kruse, F.A.; Lefkoff, A.B.; Boardman, J.W.; Heiedbrecht, K.B.; Shapiro, A.T.; Barloon, P.J.; Goetz, A.F.H. The Spectral Image Processing System (SIPS)—Interactive visualization and analysis of imaging spectrometer data. *Remote Sens. Environ.* **1993**, *44*, 145–163.
22. De Carvalho Júnior, O.A.; Meneses, P.R. Spectral Correlation Mapper (SCM): An Improving Spectral Angle Mapper. In Proceedings of Annual JPL Airborne Earth Science Workshop, Pasadena, CA, USA, 23–25 February 2000; pp. 65–74.
23. Azevedo, A.C.R.; Luz, S.L.B.; Vilela, M.L.; Rangel, E.F. Studies on the sandfly fauna of Samuel ecological station Porto Velho municipality, Rondônia State, Brazil. *Mem. Inst. Oswaldo Cruz* **1993**, *88*, 509–512.
24. Luz, S.L.B.; Lourenço-de-Oliveira, R. Forest Culicinae mosquitoes in the environs of Samuel hydroelectric plant, State of Rondônia, Brazil. *Mem. Inst. Oswaldo Cruz* **1996**, *91*, 427–432.
25. Skole, D.; Tucker, C. Evidence for tropical deforestation, fragmented habitat, and adversely affected habitat in the Brazilian Amazon: 1978–1988. *Science* **1993**, *260*, 1905–1910.

26. Laurance, W.F.; Lovejoy, T.E.; Vasconcelos, H.L.; Bruna, E.M.; Didham, R.K.; Stouffer, P.C.; Gascon, C.; Bierregaard, R.O.; Laurance, S.G.; Sampaio, E. Ecosystem decay of Amazonian Forest fragments: A 22-year investigation. *Conserv. Biol.* **2002**, *16*, 605–618.
27. Rosenqvist, A.; Shimada, M.; Ito, N.; Watanabe, M. ALOS PALSAR: A pathfinder mission for global-scale monitoring of the environment. *IEEE Trans. Geosci. Remote Sens.* **2007**, *45*, 3307–3316.
28. Almeida Filho, R.; Shimabukuro, Y.E.; Rosenqvist, A.; Sanchez, G.A. Using dual polarized ALOS PALSAR data for detecting new fronts of deforestation in the Brazilian Amazônia. *Int. J. Remote Sens.* **2009**, *30*, 3735–3743.
29. Walker, W.S.; Stickler, C.M.; Kellndorfer, J.M.; Kirsch, K.M.; Nepstad, D.C. Large-area classification and mapping of forest and land cover in the Brazilian Amazon: A comparative analysis of ALOS/PALSAR and Landsat data sources. *IEEE J. Sel. Top. Appl. Earth Obs. Remote Sens.* **2010**, *3*, 594–604.
30. Green, R.O.; Eastwood, M.L.; Sarture, C.M.; Chrien, T.G.; Aronson, M.; Chippendale, B.J.; Faust J.A.; Pavri, B.E.; Chovit, C.J.; Solis, M.; *et al.* Imaging spectroscopy and the Airborne Visible/Infrared Imaging Spectrometer (AVIRIS). *Remote Sens. Environ.* **1998**, *65*, 227–248.
31. Green, A.A.; Berman, M.; Switzer, P.; Craig, M.D. A transformation for ordering multispectral data in terms of images quality with implications for noise removal. *IEEE Trans. Geosci. Remote Sens.* **1988**, *6*, 65–74.
32. Lee, J.B.; Woodyatt, A.S.; Berman, M. Enhancement of high spectral resolution remote sensing data by a noise—Adjusted principal components transform. *IEEE Trans. Geosci. Remote Sens.* **1990**, *28*, 295–304.
33. Dickson, B.; Taylor, G. Noise reduction of aerial gamma-ray survey. *Explor. Geophys.* **1988**, *29*, 324–329.
34. Dickson, B.L.; Taylor, G.F. Maximum noise fraction method reveals detail in aerial gamma-ray surveys. *Explor. Geophys.* **2000**, *31*, 73–77.
35. De Carvalho Júnior, O.A.; Hermuche, P.M.; Guimarães, R.F. Identificação regional da floresta decidual na bacia do rio Paranã a partir da análise multitemporal de imagens MODIS. *Rev. Bras. Geofís.* **2006**, *24*, 319–332.
36. De Carvalho Júnior, O.A.; Sampaio, C.S.; da Silva, N.C.; Couto Júnior, A.F.; Gomes, R.A.T.; de Carvalho, A.P.F.; Shimabukuro, Y.E. Classificação de padrões de savana usando assinaturas temporais NDVI do sensor MODIS no Parque Nacional Chapada dos Veadeiros. *Rev. Bras. Geofís.* **2008**, *26*, 1–13.
37. De Carvalho Junior, O.A.; da Silva, N.C.; de Carvalho, A.P.F.; Couto Júnior, A.F.; Silva, C.R.; Shimabukuro, Y.E.; Guimarães, R.F.; Gomes, R.A.T. Combining noise-adjusted principal components transform and median filter techniques for denoising MODIS temporal signatures. *Rev. Bras. Geofís.* **2012**, *30*, 147–157.
38. Switzer, P.; Green, A.A. *Min/Max Autocorrelation Factors for Multivariate Spatial Imaging*; Technical Report No. 6; Stanford University: Stanford, CA, USA, 1984.
39. Bateson, C.A.; Curtiss, B. A method for manual endmember selection and spectral unmixing. *Remote Sens. Environ.* **1996**, *55*, 229–243.

40. Bateson, C.A.; Asner, G.P.; Wessman, C.A. Endmember bundles: A new approach to incorporating endmember variability into spectral mixture analysis. *IEEE Trans. Geosci. Remote Sens.* **2000**, *38*, 1083–1094.
41. Berman, M.; Kiiiveri, H.; Ryan, L.; Ernst, A.; Dunne, R.; Huntington, J.F. ICE: A statistical approach to identifying endmembers in hyperspectral images. *IEEE Trans. Geosci. Remote Sens.* **2004**, *42*, 1–11.
42. Tompkins, S.; Mustard, J.F.; Pieters, C.M.; Forsyth, D.W. Optimization of endmembers mixture analysis for spectral. *Remote Sens. Environ.* **1997**, *59*, 472–489.
43. Winter, M. N-FINDR: An Algorithm for Fast Autonomous Spectral End-Member Determination in Hyperspectral Data. In Proceedings of the SPIE Conference on Imaging Spectrometry V, Denver, CO, USA, 27 October 1999; Volume 3753, pp. 266–275.
44. Boardman, J.W.; Kruse, F.A. Automated Spectral Analysis: A Geologic Example Using AVIRIS Data, North Grapevine Mountains, Nevada. In Proceedings of the ERIM–Tenth Thematic Conference on Geologic Remote Sensing, San Antonio, TX, USA, 9–12 May 1994; pp. I-407–I-418.
45. ENVI. *The Environment for Visualizing Images Users Guide*, 4th ed.; Research Systems Inc.: Boulder, CO, USA, 2000; p. 930.
46. Adams, J.B.; Gillespie, A.R. *Remote Sensing of Landscapes with Spectral Images. A Physical Modeling Approach*; Cambridge University Press: New York, NY, USA, 2006; p. 362.
47. Jensen, J.R. *Introductory Digital Image Processing*; Prentice-Hall: Englewood Cliffs, NJ, USA, 1986.
48. Congalton, R.; Green, K. *Assessing the Accuracy of Remotely Sensed Data: Principles and Practices*; CRC/Lewis Press: Boca Raton, FL, USA, 1999.
49. Campbell, F.W.; Robson, J.G. Application of Fourier analysis to the visibility of gratings. *J. Physiol.* **1968**, *197*, 551–566.
50. Jain, A.K.; Farrokhnia, F. Unsupervised texture segmentation using Gabor filters. *Pattern Recognit.* **1991**, *24*, 1167–1186.
51. Haralick, R.M.; Shanmugan K.; Dinstein, I. Textural features for image classification. *IEEE Trans. Syst. Man-Cybern.* **1973**, *3*, 610–621.
52. Haralick, R.M. Statistical and structural approaches to texture. *Proc. IEEE* **1979**, *67*, 786–804.
53. Chai, H.Y.; Wee, L.K.; Swee, T.T.; Salleh, S.H.; Ariff, A.K. Gray-level co-occurrence matrix bone fracture detection. *Am. J. Appl. Sci.* **2011**, *8*, 26–32.
54. Ou, X.; Pan, W.; Xiao, P. *In vivo* skin capacitive imaging analysis by using grey level co-occurrence matrix (GLCM). *Int. J. Pharm.* **2014**, *460*, 28–32.
55. Rajendra Acharya, U.; Dua, S.; Du, X.; Vinitha Sree, S.; Chua, C.K. Automated diagnosis of glaucoma using texture and higher order spectra features. *Trans. Inf. Technol. Biomed.* **2011**, *15*, 449–455.
56. Su, T.L.; Lu, C.F. Automated vision system for recognising Lycra Spandex Defects. *Fibres Text. East. Eur.* **2011**, *19*, 43–46.
57. Wang, S.W.; Su, T.L. An identification system for classifying nonwoven quality. *Appl. Mech. Mater.* **2013**, *241*, 466–469.
58. Bianconi, F.; Ceccarelli, L.; Fernández, A.; Saetta, S.A. A sequential machine vision procedure for assessing paper impurities. *Comput. Ind.* **2014**, *65*, 325–332.

59. Champion, I.; Dubois-Fernandez, P.; Guyon, D.; Cottrel, M. Radar image texture as a function of forest stand age. *Int. J. Remote Sens.* **2008**, *29*, 1795–1800.
60. Li, P.; Fang, S. SAR image classification based on its texture features. *Geo-Spat. Inf. Sci.* **2003**, *6*, 16–19.
61. Gupta, M.; Bhaskar, D.; Bera, R.; Biswas, S. Target detection of ISAR data by principal component transform on co-occurrence matrix. *Pattern Recog. Lett.* **2012**, *33*, 1682–1688.
62. Barber, D.G.; Ledrew, E.F. SAR sea ice discrimination using texture statistics: A multivariate approach. *Photogramm. Eng. Remote Sens.* **1991**, *57*, 385–395.
63. Dell’Acqua, F.; Gamba, P. Discriminating urban environments using multiscale texture and multiple SAR images. *Int. J. Remote Sens.* **2006**, *27*, 3797–3812.
64. Holmes, Q.A.; Nuesch, D.R.; Shuchman, R.A. Textural analysis and real-time classification of sea-ice types using digital SAR data. *IEEE Trans. Geosci. Remote Sens.* **1984**, *22*, 113–120.
65. Shokr, M.E. Evaluation of second-order texture parameters for sea ice classification from radar images. *J. Geophys. Res.* **1991**, *96*, 10625–10640.
66. Soh, L.-K.; Tsatsoulis, C. Texture analysis of SAR sea ice imagery using gray level co-occurrence matrices. *IEEE Trans. Geosci. Remote Sens.* **1999**, *37*, 780–795.
67. Weszka, J.; Dyer, C.; Rosenfeld, A. A comparative study of texture measures for terrain classification. *IEEE Trans. Syst. Man-Cybern.* **1976**, *6*, 269–285.
68. Clausi, D.A. An analysis of co-occurrence texture statistics as a function of grey level quantization. *Can. J. Remote Sens.* **2002**, *28*, 45–62.
69. Clausi, D.A.; Yue, B. Comparing cooccurrence probabilities and Markov random fields for texture analysis of SAR sea ice imagery. *IEEE Trans. Geosci. Remote Sens.* **2004**, *42*, 215–228.
70. Karathanassi, V.; Iossifidis, C.; Rokos, D. A texture-based classification method for classifying built areas according to their density. *Int. J. Remote Sens.* **2000**, *21*, 1807–1823.
71. Zhang, Q.; Wang, J.; Gong, P.; Shi, P. Study of urban spatial patterns from SPOT panchromatic imagery using textural analysis. *Int. J. Remote Sens.* **2003**, *24*, 4137–4160.
72. Marceau, D.J.; Gratton, D.J.; Fournier, R.A.; Fortin, J.-P. Remote sensing and the measurement of geographical entities. 2. The optimal spatial resolution. *Remote Sens. Environ.* **1994**, *49*, 105–117.
73. Puissant, A.; Hirsch, J.; Weber, C. The utility of texture analysis to improve perpixel classification for high to very high spatial resolution imagery. *Int. J. Remote Sens.* **2005**, *26*, 733–745.
74. Franklin, S.E.; Wulder, M.A.; Gerylo, G.R. Texture analysis of IKONOS panchromatic data for Douglas-fire forest age class separability in British Columbia. *Int. J. Remote Sens.* **2001**, *22*, 2627–2632.
75. Kiema, J.B.K. Texture analysis and data fusion in the extraction of topographic objects from satellite imagery. *Int. J. Remote Sens.* **2002**, *23*, 767–776.
76. Anvs, H.; Bannari, A.; He, D.C.; Morin, D. Texture Analysis for the Mapping of Urban Areas Using Airborne MEIS-II Images. In Proceedings of the First International Airborne Remote Sensing Conference and Exhibition (ERIM), Strasbourg, France, 11–15 September 1994; Volume 3, pp. 231–245.
77. Baraldi, A.; Parmiggiani, F. An investigation of the textural characteristics associated with gray level cooccurrence matrix statistical parameters. *IEEE Trans. Geosci. Remote Sens.* **1995**, *33*, 293–304.

78. Clausi, D.A. Comparison and fusion of co-occurrence, Gabor and MRF texture features for classification of SAR sea-ice imagery. *Atmosphere-Ocean* **2001**, *39*, 183–194.
79. Sali, E.; Wolfson, H. Texture classification in aerial photographs and satellite data. *Int. J. Remote Sens.* **1992**, *13*, 3395–3408.
80. Clausi, D.A.; Zhao, Y. Rapid extraction of image texture by co-occurrence using a hybrid data structure. *Comput. Geosci.* **2002**, *28*, 763–774.
81. Wei, L.; Hu, Z.; Guo, M.; Jiang, M.; Zhang, S. Texture Feature Analysis in Oil Spill Monitoring by SAR Image. In Proceedings of IEEE 20th International Conference on Geoinformatics (GEOINFORMATICS), Hong Kong, China, 15–17 June 2012; pp. 1–6.
82. Su, W.; Li, J.; Chen, Y.; Liu, Z.; Zhang, J.; Low, T.M.; Suppiah, I.; Hashim, S.A.M. Textural and local spatial statistics for the object oriented classification of urban areas using high resolution imagery. *Int. J. Remote Sens.* **2008**, *29*, 3105–3117.
83. Perez, C.A.; Cament, L.A.; Castillo, L.E. Methodological improvement on local Gabor face recognition based on feature selection and enhanced Borda count. *Pattern Recognit.* **2011**, *44*, 951–963.
84. Wang, X.; Ding, X.; Liu, C. Gabor filters-based feature extraction for character recognition. *Pattern Recognit.* **2005**, *38*, 369–379.
85. Grigorescu, S.E.; Petkov, N.; Kruizinga, P. Comparison of texture features based on Gabor filters. *IEEE Trans. Image Process.* **2002**, *11*, 1160–1167.
86. Petkov, N.; Kruizinga, P. Computational models of visual neurons specialized in the detection of periodic and aperiodic oriented visual stimuli: Bar and grating cells. *Biol. Cybern.* **1997**, *76*, 83–96.
87. Petkov, N. Biologically motivated computationally intensive approaches to image pattern recognition. *Future Gen. Comput. Syst.* **1995**, *11*, 451–465.
88. De Valois, R.L.; Albrecht, D.G.; Thorell, L.G. Spatial frequency selectivity of cells in macaque visual cortex. *Vis. Res.* **1982**, *22*, 545–559.
89. Bianconi, F.; Fernández, A. Evaluation of the effects of Gabor filter parameters on texture classification. *Pattern Recognit.* **2007**, *40*, 3325–3335.
90. Kumar, A.; Pang, G.K. Defect detection in textured materials using Gabor filters. *IEEE Trans. Ind. Appl.* **2002**, *38*, 425–440.
91. Clausi, D.A.; Deng, H. Design-based texture feature fusion using Gabor filters and co-occurrence probabilities. *IEEE Trans. Image Process.* **2005**, *14*, 925–936.
92. Jain, A.K.; Ratha, N.R.; Laksmanan, S. Object detection using Gabor filters. *Pattern Recognit.* **1997**, *30*, 295–309.
93. Li, S.; Shawe-Taylor, J. Comparison and fusion of multiresolution features for texture classification. *Pattern Recognit. Lett.* **2004**, *26*, 633–638.
94. Manjunath, B.S.; Ma, W.Y. Texture features for browsing and retrieval of image data. *IEEE Trans. Pattern Anal. Mach. Intell.* **1996**, *18*, 837–841.
95. Turner, M.R. Texture discrimination by Gabor functions. *Biol. Cybern.* **1986**, *55*, 71–82.
96. Clausi, D.A.; Jernigan, M.E. Designing Gabor filters for optimal texture separability. *Pattern Recognit.* **2000**, *33*, 1835–1849.
97. Spitzer, H.; Hochstein, S. A complex-cell receptive-field model. *J. Neurosci.* **1985**, *53*, 1266–1286.

98. Bioucas-Dias, J.M.; Nascimento, J.M. Hyperspectral subspace identification. *IEEE Trans. Geosci. Remote Sens.* **2008**, *46*, 2435–2445.
99. Lu, R. Detection of bruises on apples using near-infrared hyperspectral imaging. *Trans.-Am. Soc. Agric. Eng.* **2003**, *46*, 523–553
100. Underwood, E.; Ustin, S.; DiPietro, D. Mapping nonnative plants using hyperspectral imagery. *Remote Sens. Environ.* **2003**, *86*, 150–161.
101. Yang, C.; Everitt, J.H.; Fletcher, R.S.; Jensen, R.R.; Mausel, P.W. Evaluating AISA+ hyperspectral imagery for mapping black mangrove along the South Texas Gulf Coast. *Photogram. Eng. Remote Sens.* **2009**, *75*, 425–435.
102. Dickson, B.L. Recent advances in aerial gamma-ray surveying. *J. Environ. Radioact.* **2004**, *76*, 225–236.
103. Billings, S.D.; Brian, R.M.; Garry, N.N. Deconvolution and spatial resolution of airborne gamma-ray surveys. *Geophysics* **2003**, *68*, 1257–1266.

© 2014 by the authors; licensee MDPI, Basel, Switzerland. This article is an open access article distributed under the terms and conditions of the Creative Commons Attribution license (<http://creativecommons.org/licenses/by/3.0/>).